Acta Pharmaceutica Sinica B 2026;16(3):1584−1604

Chinese Pharmaceutical Association
Institute of Materia Medica, Chinese Academy of Medical Sciences

Acta Pharmaceutica Sinica B

www.elsevier.com/locate/apsb
www.sciencedirect.com

ORIGINAL ARTICLE

A triple combination strategy for nasopharyngeal carcinoma: Aptamer-guided liposomal chemotherapy, engineered NK cells, and Fc-enhanced PD-L1 antibody therapy

Chaoyan Yao[a,b,c,d,e], Lei Wang[a,c,e], Weidong Liu[a,c,e], Ning Shi[a,b,c,d,e], Ziling Liao[c,e], Yuxuan Fu[c,e], Jinhao Ouyang[c,e], Xuan Lei[c,e], Qianping Huang[b,c,e], Siyu Li[c], Yihua Zhouyang[b], Pinnan Zhao[b], Jie Wang[b], Hongjuan Xu[a,c,d,e,f], Wenhu Zhou[g], Xingjun Jiang[a,d,*], Xiang Gao[b,*], Caiping Ren[a,c,d,e,*], Longlong Luo[b,*]

[a]*Department of Neurosurgery, Xiangya Hospital, Central South University, Changsha 410008, China*
[b]*Academy of Military Medical Sciences, Beijing 100850, China*
[c]*Cancer Research Institute, Xiangya School of Basic Medical Science, Central South University, Changsha 410078, China*
[d]*National Clinical Research Center for Geriatric Disorders, Xiangya Hospital, Central South University, Changsha 410008, China*
[e]*The NHC Key Laboratory of Carcinogenesis and the Key Laboratory of Carcinogenesis and Cancer Invasion of the Chinese Ministry of Education, Central South University, Changsha 410078, China*
[f]*NHC Key Laboratory of Biological Nanotechnology, Xiangya Hospital, Central South University, Changsha 410008, China*
[g]*Xiangya School of Pharmaceutical Sciences, Central South University, Changsha 410013, China*

Received 13 August 2025; received in revised form 28 September 2025; accepted 29 September 2025

KEY WORDS

Nasopharyngeal carcinoma (NPC);

Abstract The effective treatment of nasopharyngeal carcinoma (NPC) is challenged by an immunosuppressive tumor microenvironment (TME) and insufficient immune effector cell activation. Herein, we design a synergistic tri-modal therapeutic strategy to overcome these barriers. This platform integrates: (1) a CD109-targeted liposomal doxorubicin (S3-Lip-DOX) for precise chemotherapy and induction of

*Corresponding authors.
E-mail addresses: jiangxj@csu.edu.cn (Xingjun Jiang), gaoxiang609@163.com (Xiang Gao), rencaiping@csu.edu.cn (Caiping Ren), luolong_long@126.com (Longlong Luo).

Peer review under the responsibility of Chinese Pharmaceutical Association and Institute of Materia Medica, Chinese Academy of Medical Sciences.

https://doi.org/10.1016/j.apsb.2025.10.007

Chemo-immunotherapy;
Triple-combination therapy;
Liposomal doxorubicin;
Aptamer-engineered NK cells;
ADCC;
CD109;
PD-L1

immunogenic cell death (ICD); (2) non-genetically engineered natural killer (NK) cells armed with dual aptamers (targeting CD109 and PD-L1) *via* bio-orthogonal chemistry for enhanced tumor recognition (S3-P-NK); and (3) an Fc-engineered anti-PD-L1 antibody (Atezolizumab/IgG1) that restores antibody-dependent cellular cytotoxicity (ADCC). Crucially, we uncovered a key mechanistic synergy: S3-Lip-DOX treatment, as a stress-adaptive response, upregulates PD-L1 expression on NPC cells. This finding provides a compelling rationale for the integration, turning a potential immune escape mechanism into a therapeutic vulnerability. The complete regimen, comprising S3-Lip-DOX, S3-P-NK, and Atezolizumab/IgG1, demonstrated potent synergistic antitumor effects *in vitro* and *in vivo*. This triple-combination therapy not only achieved significant tumor regression but also robustly reprogrammed the innate tumor microenvironment, evidenced by enhanced dendritic cell (DC) maturation and pro-inflammatory macrophage activation. This work establishes a mechanism-driven, modular therapeutic platform that effectively coordinates targeted chemotherapy with innate immunotherapy, holding significant translational potential for solid tumors.

1. Introduction

Nasopharyngeal carcinoma (NPC), a malignancy with a high prevalence in Southeast Asia and southern China, presents significant therapeutic challenges[1,2]. While doxorubicin (DOX), a topoisomerase II inhibitor, is a potent chemotherapeutic agent, its clinical application is severely hampered by dose-limiting systemic toxicities, including cardiotoxicity and nephrotoxicity[3-6]. Liposomal formulations have been developed to mitigate these off-target effects, leveraging favorable biocompatibility and improved pharmacokinetics[7-9]. However, conventional liposomes primarily rely on the enhanced permeability and retention (EPR) effect for tumor accumulation, a passive mechanism often compromised by the heterogeneous vasculature of solid tumors like NPC[10-12]. To enable active, ligand-directed targeting, we previously identified a high-affinity DNA aptamer, S3, that specifically recognizes CD109, a tumor-associated surface antigen on NPC cells[13,14]. This forms the basis for our first therapeutic module: S3-conjugated liposomal DOX (S3-Lip-DOX), designed for precision chemotherapy.

Complementing chemotherapy, immunotherapy has emerged as a transformative cancer treatment paradigm. Natural killer (NK) cells, capable of eliminating tumor cells without prior sensitization, are promising effectors for adoptive cell therapy[15-17]. Nevertheless, the efficacy of unmodified NK cells is often limited by poor tumor-specific recognition[18]. While chimeric antigen receptor (CAR)-NK cells can enhance specificity, their development is associated with challenges including insertional mutagenesis risks, complex manufacturing, and high costs[19,20]. As a non-genetic and highly versatile alternative, aptamer-based surface engineering offers a powerful solution[21-23]. By employing metabolic glycan labeling and bio-orthogonal click chemistry, we can anchor targeting aptamers directly onto the NK cell surface, conferring tumor-homing capabilities without genetic modification[24,25]. This leads to our second module: dual-aptamer engineered NK cells (S3-P-NK), programmed to recognize both CD109 and the critical immune checkpoint PD-L1.

To further amplify the therapeutic potency, we sought to maximize NK cell-mediated cytotoxicity. The clinical anti-PD-L1 antibody, Atezolizumab, is engineered with an Fc-silencing mutation (N297A) to abrogate ADCC[26,27]. However, emerging evidence suggests that preserving Fc effector functions can be therapeutically advantageous[28-30]. Therefore, our third module incorporates an Fc-active of wild type IgG1, Atezolizumab/IgG1, designed to engage FcγRIIIa on our engineered NK cells and unleash a potent ADCC response, creating a powerful synergistic axis with the PD-L1 aptamer targeting.

A pivotal finding of our study provides the central mechanistic rationale for integrating these three modules. We discovered that treatment with S3-Lip-DOX induces a stress-adaptive upregulation of PD-L1 on NPC cells. Instead of being a therapeutic obstacle, this chemotherapy-induced immune escape signature presents an actionable vulnerability. It creates an ideal scenario where S3-Lip-DOX not only delivers a direct cytotoxic payload but also "paints" the tumor with the very target (PD-L1) that our subsequent immunotherapies are designed to attack. This insight allows us to orchestrate a synergistic cascade: S3-Lip-DOX initiates targeted killing and upregulates PD-L1, which is then concertedly engaged by both the PD-L1 aptamer on S3-P-NK cells for recognition and the Atezolizumab/IgG1 for potent ADCC-mediated elimination.

In this study, we designed and validated this triple-combination strategy for NPC (Scheme 1). We hypothesized that by rationally coordinating targeted chemotherapy, non-genetic cell engineering, and Fc-enhanced checkpoint blockade, we could achieve profound synergistic antitumor efficacy. Here, we demonstrate that this multi-modal platform not only suppresses tumor growth effectively but also reshapes the innate immune microenvironment. This work establishes a scalable and programmable therapeutic framework that transforms a chemotherapy-induced adaptive response into a potent immunological trigger, offering a promising paradigm for treating solid tumors.

2. Materials and methods

2.1. Chemicals and reagents

All aptamer sequences used in this study were synthesized and HPLC-purified by Sangon Biotech (Shanghai, China), with detailed sequences provided in Supporting Information Table S1. Lipid components including 1,2-distearoyl-*sn*-glycero-3-phosphocholine (DSPC) (S01005), cholesterol (O01001), DSPE-PEG_{2000}(F01008), and DSPE-PEG_{2000}-COOH (F07004) were purchased from AVT

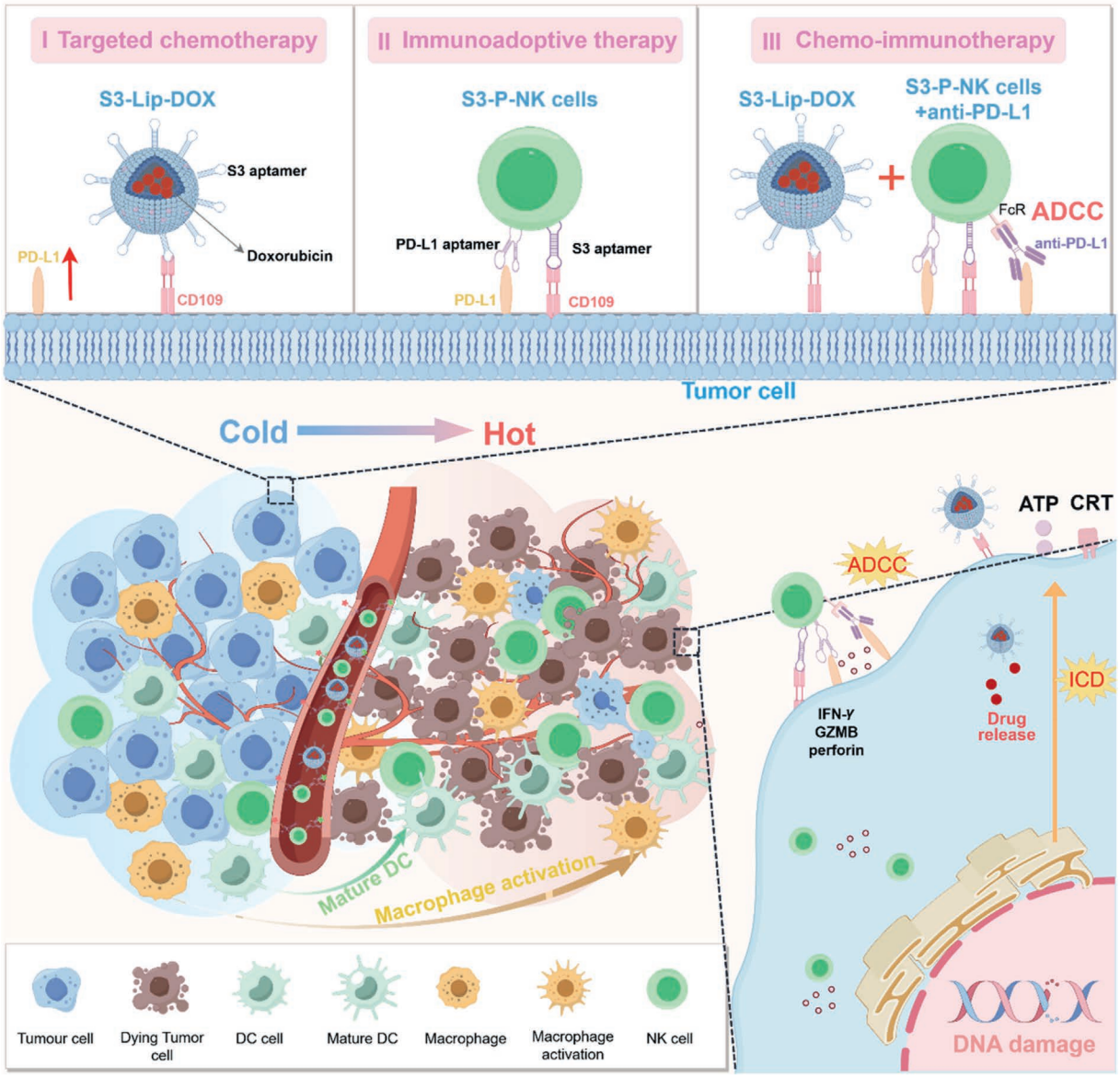

Scheme 1 A synergistic chemo-immunotherapy cascade for NPC. Targeted chemotherapy (S3-Lip-DOX) induces immunogenic cell death and PD-L1 upregulation, which are thus synergistically targeted by dual-aptamer NK cells (S3-P-NK) and ADCC to reverse immunosuppression and eliminate the tumor.

Pharmaceutical Tech Co., Ltd. (Shanghai, China). All other chemicals and organic solvents used for synthesis were obtained from Aladdin Reagent Co., Ltd. (Shanghai, China), unless otherwise specified. *N*-Azidoacetylmannosamine-tetraacylated (Ac_4ManNAz) (361154-30-5) from Sigma−Aldrich (St. Louis, MO, USA), and recombinant human IL-2 (042212) from Peprotech (Rocky Hill, NJ, USA). The Annexin V-PE/7-AAD apoptosis detection kit (CA1030) were purchased from Servicebio (Wuhan, China). Doxorubicin (DOX, D8740), and the TUNEL apoptosis detection kit (T2130) were purchased from Solarbio (Beijing, China). The near-infrared dye DIR (BMD0074), the Cell Counting Kit-8 (CCK-8) (498/1000T), CheKine™ Micro Lactate Dehydrogenase (LDH) Assay Kit (639/96 T/96 S), and CheKine™ Micro ATP Content Assay Kit (358/48 T/48 S) were obtained from Abbkine (Wuhan, China). ELISA kits for human IFN-γ (CSB-E08636h), granzyme B (CSB-E08718h), and perforin (CSB-E09313h) were acquired from Cusabio (Wuhan, China). Primary antibodies against human calreticulin (27298-1-AP), Bax (50599-2-Ig), and Bcl-2 (12789-1-AP), Ki67 (27309-1-AP) and PD-L1 (17952-1-AP) were purchased from Proteintech Group, Inc. (Wuhan, China), human cleaved caspase3 (#9661) and caspase3 (#14220) were purchased from Cell Signaling Technology (Beverly, MA, USA), and HRP-conjugated goat anti-rabbit IgG (ZB-2301) and goat anti-mouse IgG (ZB-2305) were obtained from Zhongshan Golden Bridge Biotechnology Co., Ltd. (Beijing, China).

2.2. *Cell lines and animals*

The human NPC cell lines 5-8F and C666-1 were cultured in RPMI-1640 medium (Gibco, C11875500BT, Carlsbad, CA, USA) supplemented with 10% fetal bovine serum (FBS; Gibco). Normal nasopharyngeal epithelial NP69 cells were maintained in

keratinocyte serum-free medium (KSFM) (ThermoFisher, 10744019, Carlsbad, CA, USA). The NK-92 cell line was obtained from the American Type Culture Collection (ATCC, Manassas, VA, USA) and cultured in α-MEM (C12571500BT, Gibco, Carlsbad, CA, USA) supplemented with 12.5% FBS (Gibco), 12.5% horse serum (Gibco), and 200 U/mL recombinant human interleukin-2 (Peprotech). All cell lines were incubated at 37 °C in a humidified atmosphere containing 5% CO_2.

BALB/c nude mice (male, 5−6 weeks old, 18−20 g) were purchased from Beijing Weitong Lihua Experimental Animal Technology Co., Ltd. (Beijing, China). All experimental procedures were executed according to the protocols approved by the Animal Care and Use Committee of Central South University (approval number: 2021-XMSB-0162) and conducted in accordance with institutional ethical guidelines. Mice were housed under specific pathogen-free (SPF) conditions with controlled temperature (23 ± 2 °C), relative humidity (60 ± 5%), and a 12 h light/dark cycle, with free access to food and water.

2.3. Preparation of S3-Lip-DOX

S3-Lip-DOX nanoparticles were prepared *via* a two-step process. First, doxorubicin-loaded liposomes (Lip-DOX) were fabricated using the thin-film hydration method[31]. Briefly, DSPC, cholesterol, and DSPE-PEG_{2000} were dissolved in chloroform at a mass ratio of 10:5:1 and transferred into a round-bottom flask to form a uniform solution. The organic solvent was evaporated under reduced pressure to form a thin lipid film, which was subsequently hydrated with ammonium sulfate solution at 65 °C for 30 min. The resulting liposomal suspension was sonicated and extruded through polycarbonate membranes with pore sizes of 450 nm and 220 nm (Merck Millipore, Burlington, MA, USA) to obtain liposomes of uniform size. Free ammonium sulfate was removed by dialysis, DOX was then actively loaded into the liposomes *via* the ammonium sulfate gradient method to obtain Lip-DOX nanoparticles.

In the second step, the S3 aptamer was covalently conjugated to DSPE-PEG_{2000}-COOH to synthesize DSPE-PEG_{2000}-S3, using EDC and NHS as coupling agents. The reaction was carried out at room temperature, and unreacted reagents were removed by dialysis. The purified DSPE-PEG_{2000}-S3 was then post-inserted into the preformed Lip-DOX by incubation at 60 °C for 1 h, resulting in the final aptamer-functionalized nanocarrier, S3-Lip-DOX.

2.4. Characterization of S3-Lip-DOX

The particle size, polydispersity index (PDI), and zeta potential of S3-Lip-DOX were measured using a Zetasizer (Malvern, UK) at 25 °C after dilution in PBS. The morphology of nanoparticles was visualized by transmission electron microscopy (TEM; JEOL JEM-2010, Tokyo, Japan) following negative staining with 2% phosphotungstic acid (*w/v*, pH 7.0). To determine encapsulation efficiency (EE%) and drug loading (DL%), nanoparticles were lysed with anhydrous ethanol, and the absorbance of DOX was measured at 480 nm using a UV−Vis spectrophotometer (UV-2600, Shimadzu, Kyoto, Japan). The relevant calculations were carried out according to Eqs. (1) and (2):

$$\text{EE}\ (\%) = W_{\text{Encapsulated}}/W_{\text{Drug}} \times 100 \quad (1)$$

$$\text{DL}\ (\%) = W_{\text{Encapsulated}}/W_{\text{Total}} \times 100 \quad (2)$$

where $W_{\text{Encapsulated}}$ is the drug mass contained in the liposomes, W_{Drug} is the total amount of DOX added, and W_{total} is the total weight of the liposomes and the sum of the drug mass.

The colloidal stability of S3-Lip-DOX was assessed by monitoring particle size and PDI at predetermined intervals after storage in PBS at 4 °C and in PBS containing 10% FBS at 37 °C[32]. The *in vitro* release profile of the liposomes was investigated employing the dialysis method[33]. Briefly, 1 mL of S3-Lip-DOX suspension was sealed in a dialysis bag (Spectrum Labs, 3.5 kDa MWCO, Rancho Dominguez, CA, USA) and immersed in 5 mL of PBS (pH 7.4). The release system was incubated at 37 °C in a shaking water bath (Thermo Scientific, SHKA4000, Waltham, MA, USA) at 120 rpm under light-protected conditions. At predetermined time intervals (1, 2, 6, 12, 24, 48, 60, and 72 h), 3 mL of release medium was withdrawn and replaced with fresh preheated buffer to maintain sink conditions. The cumulative release of DOX was quantified at 480 nm by UV-Vis spectrophotometry (Shimadzu).

2.5. Cellular uptake of S3-Lip-DOX by NPC cells

NP69, 5-8F, and C666-1 cell lines were seeded into 12-well plates and cultured overnight at 37 °C in a 5% CO_2 incubator. Subsequently, the cells underwent washing with PBS and were then exposed to free DOX, Lip-DOX and S3-Lip-DOX at a concentration of 10 μg/mL for a duration of 6 h. Following this treatment, the cells were washed three times with PBS and fixed with 4% paraformaldehyde at room temperature for 30 min. The cell nuclei were stained using 4′,6-diamidino-2-phenylindole (DAPI; Beyotime, C1002, Shanghai, China), and the samples were analyzed using an inverted fluorescence microscope (Nikon, Tokyo, Japan). Additionally, NP69, 5-8F, and C666-1 cells were independently subjected to the same 6 h treatment and subsequently collected for analysis *via* flow cytometry.

2.6. Targeting destruction of NPC cells by S3-Lip-DOX

To assess the cytotoxicity of nanocarriers, blank liposomes and DSPE-PEG-S3 were incubated with NP69, 5-8F, and C666-1 cells. Cell viability was determined using the CCK-8 following the manufacturer's instructions.

To evaluate the antiproliferative effect of S3-Lip-DOX, NP69, 5-8F, and C666-1 cells were seeded into 96-well plates at a density of 6×10^3 cells per well in 200 μL of complete medium and incubated overnight at 37 °C in a humidified 5% CO_2 incubator. The medium was then replaced with 200 μL of fresh medium containing free DOX, Lip-DOX, or S3-Lip-DOX at equivalent DOX concentrations. At 1-, 2-, 3-, 4-, and 5-days post-treatment, the medium was removed and replaced with 100 μL of fresh medium containing 10% CCK-8 reagent. After incubation for 2 h at 37 °C in the dark, absorbance was measured at 450 nm using a microplate reader (BioTek, Synergy H1, Winooski, VT, USA), and cell growth curves were plotted accordingly.

To assess apoptosis induction, NP69, 5-8F, and C666-1 cells were treated with free DOX, Lip-DOX, or S3-Lip-DOX for 48 h. Cells were then harvested, washed with cold PBS, and stained using the Annexin V-PE/7-AAD apoptosis detection kit according to the manufacturer's protocol. Apoptotic cells were quantified by flow cytometry. To further explore the underlying mechanisms,

apoptosis-related proteins were analyzed by Western blotting. Total cellular proteins samples were denatured, separated by SDS-polyacrylamide gel electrophoresis, and transferred to PVDF membranes (Merck Millipore, IPVH00010, Burlington, MA, USA). The membranes were incubated with primary antibodies at 4 °C overnight followed by HRP-conjugated secondary antibodies for 1 h at room temperature. Protein bands were detected using enhanced chemiluminescence (ECL) reagents and visualized using a Tanon imaging system (Tanon, Shanghai, China).

2.7. Biological distribution of S3-Lip-DOX in vivo

To evaluate the tumor-targeting ability of S3-Lip-DOX, BALB/c nude mice were subcutaneously injected with 2×10^6 5-8F cells to establish a xenograft model. Two weeks after tumor formation, DiR, Lip-DiR, and S3-Lip-DiR (0.5 mg/kg DiR) were administered *via* tail vein injection. Fluorescence imaging was performed at 2, 6, 12 and 24 h post-injection. At 24 h, mice were sacrificed, and major organs (heart, lungs, liver, spleen, kidneys) and tumors were collected for ex *vivo* imaging.

2.8. Therapeutic effect of S3-Lip-DOX in vivo

To evaluate the antitumor efficacy of S3-Lip-DOX, 2×10^6 5-8F cells were subcutaneously inoculated into the right flank of each BALB/c nude mouse. When tumors reached a volume of approximately 50−100 mm^3, mice were randomly divided into four groups ($n = 5$) and treated *via* tail vein injection with PBS, free DOX, Lip-DOX, or S3-Lip-DOX. A total of seven treatment sessions were administered. Tumor volume and body weight were monitored throughout the treatment period, with the tumor volume calculated as shown in Eq. (3):

$$\text{Volume} = (\text{Length} \times \text{Width}^2)/2 \quad (3)$$

At the end of the treatment, mice were euthanized, and the heart, lungs, liver, spleen, kidneys, and tumors were collected. The tumor tissue was fixed, paraffin embedded and sectioned. Tumor sections were stained with a rabbit polyclonal anti-Ki-67 antibody to assess cell proliferation. TUNEL fluorescence labeling was used to evaluate apoptosis in tumor tissues.

2.9. In vivo safety evaluation of S3-Lip-DOX

To assess the systemic safety of the treatments, mouse body weight was monitored throughout the treatment period. After the final administration, mice were euthanized, and orbital blood was collected for serum biochemical analysis, including liver function (ALT, ALB), renal function (UREA, CREA), and cardiac injury markers (CK, LDH). Major organs, including the heart, liver, spleen, lungs, and kidneys, were harvested, fixed in 4% paraformaldehyde, embedded in paraffin, sectioned at 4 μm, and stained with hematoxylin and eosin (H&E) for histopathological evaluation under an inverted microscope (Nikon).

2.10. Preparation and characterization of S3-P-NK cells

NK92 cells were incubated with 50 μmol/L Ac_4ManNAz for 24 h, followed by three washes with PBS. The cells were then incubated with DBCO-modified FAM-labeled S3 and Cy3-labeled PD-L1 aptamers in fresh medium at 37 °C for 1 h. After incubation, cells were collected by centrifugation and resuspended in PBS to obtain S3-P-NK cells for immediate use in *in vitro* and *in vivo* studies. To verify aptamer conjugation and evaluate stability, S3- and PD-L1-modified NK cells were incubated at 37 °C for 0, 2, 4, 6, 8, 12, 24, and 48 h, and fluorescence intensity was analyzed using inverted fluorescence microscopy.

For targeting evaluation, NP69 cells were used as negative controls, while 5-8F and C666-1 cells served as positive targets. S3-P-NK cells were co-cultured with target cells at an effector-to-target (*E/T*) ratio of 10:1 for 2 h. After PBS washing to remove unbound cells, adhesion of S3-P-NK cells to NP69, 5-8F, and C666-1 cells was examined by inverted fluorescence microscopy. To assess the effects of Ac_4ManNAz treatment and aptamer modification on NK cell viability, cells under different treatment conditions were cultured for 24 and 48 h, followed by viability assessment using the CCK-8 assay and flow cytometry.

2.11. The targeted cytotoxic effect of S3-P-NK cells on NPC cells

To evaluate the cytotoxicity of S3-P-NK cells toward NPC cells, NP69, 5-8F and C666-1 cells were seeded into 6-well plates at a density of 2×10^5 cells per well and incubated for 24 h under 5% CO_2. After washing with PBS, NK, S3-NK, P-NK, and S3-P-NK cells were added at an effector-to-target (*E:T*) ratio of 10:1 and co-cultured for 2 h. Unbound NK92 cells were then removed, and target cells were further incubated for 24 h. Cell viability was assessed by flow cytometry.

To determine cytokine secretion levels, NPC cells were seeded in 96-well plates at 5000 cells per well and cultured for 24 h. NK, S3-NK, P-NK, and S3-P-NK cells were co-incubated with NPC cells for 2 h, followed by removal of unbound NK cells. After an additional 24 h incubation, the culture medium was collected and centrifuged to obtain the supernatant. Levels of IFN-γ, granzyme B (GZMB), and perforin in the supernatant were quantified using enzyme-linked immunosorbent assay (ELISA) kits.

2.12. In vivo targeting of NPC xenografts by S3-P-NK cells

To evaluate the tumor-targeting capability of aptamer-modified NK cells *in vivo*, a subcutaneous xenograft model was established by inoculating nude mice subcutaneously with 2×10^6 5-8F cells. After two weeks of tumor growth, mice were intravenously injected with 5×10^6 DIR-labeled NK cells, including NK,S3-NK, P-NK, or S3-P-NK cells per mouse. Whole-body fluorescence imaging was performed at 2, 6, 12 and 24 h post-injection using an *in vivo* imaging system to monitor NK cell biodistribution. At 24 h post-injection, major organs (heart, liver, spleen, lungs, kidneys) and tumors were harvested and photographed to assess *ex vivo* fluorescence accumulation.

2.13. In vivo therapeutic efficacy of S3-P-NK cells

To evaluate the antitumor efficacy of S3-P-NK cells *in vivo*, 2×10^6 5-8F cells were subcutaneously injected into the right flank of each nude mouse. When tumors reached a volume of approximately 50−100 mm^3, mice were randomly divided into five groups ($n = 5$) and treated *via* tail vein injection with PBS, NK, S3-NK, P-NK, or S3-P-NK cells (5×10^6 cells per mouse). Each mouse also received 2000 units of IL-2 to promote NK cell survival and proliferation. A total of four treatment sessions were administered.

At the end of the study, mice were euthanized and tumors were excised, fixed in 4% paraformaldehyde, embedded in paraffin, and sectioned at a thickness of 4 μm. Immunohistochemical staining was performed using a Ki-67 primary antibody and a rabbit anti-mouse IgG secondary antibody, with 3,3′-diaminobenzidine (DAB; Sigma−Aldrich, 34002, St. Louis, MO, USA) as the chromogenic substrate. Tumor cell apoptosis was assessed using TUNEL fluorescence staining.

2.14. Safety analysis of S3-P-NK cells

To assess the systemic safety of S3-P-NK cells therapy, mouse body weight was monitored throughout the treatment period. After the final administration, mice were euthanized, and orbital blood was collected for serum biochemical analysis, including liver function (ALT, ALB), renal function (UREA, CREA), and cardiac injury markers (CK, LDH). Major organs, including the heart, liver, spleen, lungs, and kidneys, were harvested, fixed in 4% paraformaldehyde, embedded in paraffin, sectioned at 4 μm, and stained with hematoxylin and eosin (H&E) for histopathological evaluation under an inverted microscope (Nikon).

2.15. ADCC activity of S3-P-NK cells enhanced by PD-L1 antibodies

To evaluate the ADCC effects of S3-P-NK cells in the presence of PD-L1 antibodies, 5-8F cells were used as target cells. ADCC activity was assessed using a LDH release assay and a CCK-8 cell viability assay. Experimental groups included a control group, an S3-P-NK-only group, and groups treated with S3-P-NK cells in combination with various concentrations (10, 20, and 40 μg/mL) of Atezolizumab, Atezolizumab/IgG1, or avelumab.

5-8F cells were seeded into 96-well plates at a density of 6000 cells per well and cultured for 24 h. Cells were then co-incubated with S3-P-NK cells and PD-L1 antibodies at an effector-to-target (*E:T*) ratio of 5:1. At 6, 12, and 24 h post-incubation, the supernatant was collected and analyzed using an LDH Cytotoxicity Assay Kit. Absorbance at 450 nm was measured using a microplate reader. The relative LDH release was calculated as shown in Eq. (4):

$$\text{LDH release } (\%) = (\text{LDH}_{\text{Experimental}} - \text{LDH}_{\text{Background}}) / (\text{LDH}_{\text{Maximum}} - \text{LDH}_{\text{Background}}) \times 100 \quad (4)$$

In parallel, cell viability was assessed using the CCK-8 assay at the same time points. Cytotoxicity was quantified by calculating the inhibition rate as shown in Eq. (5):

$$\text{Inhibition rate } (\%) = (\text{OD}_{\text{Control}} - \text{OD}_{\text{Sample}}) / \text{OD}_{\text{Control}} \times 100 \quad (5)$$

2.16. In vitro evaluation of the combined effect of S3-Lip-DOX, S3-P-NK cells, and PD-L1 antibody

To investigate the *in vitro* efficacy of S3-Lip-DOX and S3-P-NK cells in combination with PD-L1 antibody, the experiment was divided into six groups: (1) Control group, (2) S3-P-NK cells group (*E:T* = 5:1), (3) Atezolizumab/IgG1 group (20 μg/mL), (4) S3-Lip-DOX group [IC_{50}(5-8F) = 0.72 μmol/L], (5) S3-P-NK cells combined with Atezolizumab/IgG1, and (6) S3-P-NK cells combined with Atezolizumab/IgG1 and S3-Lip-DOX. As previously described, cytotoxicity and cell viability were assessed using the LDH release assay and the CCK-8 assay, respectively.

2.17. In vivo antitumor efficacy and immune microenvironment analysis

2.17.1. Animal model and treatment regimen

All animal procedures were approved by the Institutional Animal Care and Use Committee of Central South University (approval number: 2021 XMSB 0162). Male BALB/c nude mice, 5−6 weeks old were subcutaneously inoculated in the right flank with 5×10^6 5-8F cells. When tumor volumes reached approximately 50−100 mm^3, mice were randomized ($n = 5$ per group) into six treatment groups:

G1. Control: PBS [intravenously (i.v.)]
G2. Atezolizumab/IgG1: [10 mg/kg intraperitoneally (i.p.)]
G3. S3-Lip-DOX: [2 mg/kg DOX equivalent (i.v.)]
G4. S3-P-NK cells: [5×10^6 cells/mouse (i.v.)]
G5. Combination: S3-P-NK cells + Atezolizumab/IgG1.
G6. Triple Combination: S3-P-NK cells + Atezolizumab/IgG1 + S3-Lip-DOX.

The schedule was as follows: an initial dose of S3-Lip-DOX was given alone to induce PD-L1 upregulation. This was followed by three cycles of the triple combination, where S3-Lip-DOX was administered 6 h prior to S3-P-NK and Atezolizumab/IgG1 in each cycle. Tumor volumes were measured every 4 days and calculated as shown in Eq. (6):

$$\text{Volume} = (\text{Length} \times \text{Width}^2)/2 \quad (6)$$

At the study endpoint, mice were euthanized, and tumors were excised, weighed, photographed, and processed for further analysis.

2.17.2. Flow cytometry of tumor-infiltrating leukocytes

Tumors were minced and digested in RPMI 1640 medium containing 1 mg/mL collagenase IV (Solarbio, C8160, Beijing, China) for 1 h at 37 °C to generate single-cell suspensions. The cell suspension was filtered through a 70 μm cell strainer (Corning, 431751, Corning, NY, USA). After blocking Fc receptors with anti-CD16/CD32 antibody (BD Pharmingen, 553141, San Diego, CA, USA), cells were stained with a panel of fluorochrome-conjugated antibodies: CD45-APC/Cy7 (BD, 561037, San Diego, CA, USA); F4/80-PE (BD, 565410, San Diego, CA, USA); CD11c-PE/Cy7 (BD, 561022, San Diego, CA, USA); MHC II-BV510 (BD, 562366, San Diego, CA, USA); CD86-APC (BD, 561964, San Diego, CA, USA); CD11b-FITC (BD, 561688, San Diego, CA, USA); Cell viability was assessed using 7-AAD (BD, 559925, San Diego, CA, USA). Data were acquired on a flow cytometer (BD Biosciences, San Jose, CA, USA) and analyzed using FlowJo v10 software (BD Biosciences, v10.8, New York, NY, USA). Dendritic cells (DCs) were identified as $CD45^+CD11c^+MHCII^+CD86^+$, and M1-polarized macrophages were identified as $CD45^+CD11b^+F4/80^+CD86^+$.

2.17.3. Multiplex immunofluorescence (mIF) staining

Multiplex immunofluorescence staining was performed on 4-μm-thick paraffin-embedded tumor sections using a tyramide signal amplification (TSA) kit (Servicebio, G1236, Wuhan, China) according to the manufacturer's protocol. After standard deparaffinization and rehydration, antigen retrieval was conducted in Tris-

EDTA buffer (pH 9.0) using heat-induced methods. Sections were then subjected to sequential staining cycles for three distinct antibody panels: (I) Ki67 and TUNEL; (II) F4/80, CD86, and CD206; (III) MHC II, CD11c, and CD86.

Each cycle involved incubation with a primary antibody, followed by an HRP-conjugated secondary antibody and a corresponding TSA fluorophore (488, 555, or 647). Between cycles, bound antibodies were removed *via* microwave-assisted antibody stripping. After the final cycle, nuclei were counterstained with DAPI. Images were acquired using a Nikon fluorescence microscope (Nikon, Tokyo, Japan), and the quantitative analysis of positive areas was performed with ImageJ software (National Institutes of Health, Bethesda, MD, USA).

2.18. Statistical analysis

All statistical analyses were performed using GraphPad Prism 10 (GraphPad Software, La Jolla, CA, USA). Data are expressed as mean ± standard deviation (SD). Differences between two groups were evaluated using an unpaired two-tailed Student's *t*-test. For comparisons among multiple groups, one-way analysis of variance (ANOVA) followed by Tukey's multiple comparisons test was applied. For experiments involving two independent variables, two-way ANOVA followed by Sidak's post hoc test was used. A P-value <0.05 was considered statistically significant.

3. Results

3.1. Preparation and characterization of liposomes

To construct a targeted drug delivery system, S3 aptamer-functionalized, doxorubicin-loaded liposomes (S3-Lip-DOX) were prepared *via* the post-insertion of a DSPE-PEG-S3 conjugate into pre-formed liposomes (Fig. 1A). Successful conjugation of the S3 aptamer to the liposome surface was confirmed by a gel retardation assay, where the high-molecular-weight S3-Lip-DOX complex remained in the loading well, unlike the free aptamers which migrated through the gel (Supporting Information Fig. S1).

The resulting nanoparticles exhibited ideal physicochemical properties. Transmission electron microscopy (TEM) images revealed a uniform population of spherical nanoparticles with a distinct unilamellar structure (Fig. 1B). Dynamic light scattering (DLS) analysis showed a slight but significant increase in hydrodynamic size from 188.9 ± 30.76 nm for the untargeted Lip-DOX to 208.7 ± 26.07 nm for S3-Lip-DOX (Fig. 1B). This size increase was accompanied by a shift in zeta potential from −10.16 ± 0.77 mV to a more negative value of −11.6 ± 0.71 mV, providing further evidence for the successful incorporation of the negatively charged S3 aptamer (Fig. 1C). The formulation achieved a high encapsulation efficiency (EE) of 88.8% ± 1.9% and a drug loading (DL) content of 5.92% ± 0.1% (Fig. 1D).

Critically, S3-Lip-DOX demonstrated excellent stability, a prerequisite for *in vivo* applications. The formulation showed no significant changes in particle size or polydispersity index (PDI) when stored in PBS at 4 °C for 7 days, or when incubated in PBS containing 10% fetal bovine serum (FBS) at 37 °C for 96 h, mimicking physiological conditions (Fig. 1E and F). Furthermore, *in vitro* drug release assays showed a sustained release profile, with only 35.63% of DOX released over 72 h, in stark contrast to the rapid and complete release from the free DOX solution (Fig. 1G).

Collectively, these data confirm the successful preparation of S3-Lip-DOX as a stable, high-payload drug delivery system with favorable physicochemical characteristics and sustained-release behavior.

3.2. Aptamer-mediated targeting achieves selective and enhanced uptake in NPC cells

To validate the targeting capability of our design, we assessed whether the S3 aptamer could selectively deliver its liposomal cargo into NPC cells (5-8F, C666-1) while sparing normal nasopharyngeal epithelial cells (NP69).

First, qualitative analysis by fluorescence microscopy provided a clear visual confirmation of targeting. As expected, free DOX entered all cell lines indiscriminately, resulting in strong, non-specific fluorescence. In sharp contrast, the liposomal formulations demonstrated marked selectivity. Both untargeted Lip-DOX and targeted S3-Lip-DOX showed minimal fluorescence in normal NP69 cells, suggesting that liposomal encapsulation itself reduces uptake in non-cancerous cells. The critical difference was observed in the NPC cell lines: the intracellular fluorescence was dramatically higher in cells treated with S3-Lip-DOX compared to the untargeted Lip-DOX, indicating efficient, aptamer-driven internalization (Fig. 1H).

These visual observations were then rigorously quantified by flow cytometry. The data confirmed the targeting effect with high statistical significance. The mean fluorescence intensity (MFI) in both 5-8F and C666-1 cancer cells was markedly higher for the S3-Lip-DOX group compared to the Lip-DOX group ($P < 0.01$). Crucially, this enhancement was entirely absent in normal NP69 cells, where no significant difference in MFI was observed between the two liposomal formulations (Fig. 1I).

Collectively, these results unequivocally demonstrate that the S3 aptamer functions as a highly effective and specific targeting ligand, mediating enhanced delivery of the liposomal payload specifically into NPC cells.

3.3. S3-Lip-DOX induces selective cytotoxicity, apoptosis, and immunogenic cell death in NPC cells

The cytotoxic effects of S3-Lip-DOX were evaluated in NPC and normal nasopharyngeal cells. Control experiments showed that blank liposomes and free S3 aptamers had negligible effects on the viability of any cell line tested (Supporting Information Fig. S2). Dose−response analysis revealed the half-maximal inhibitory concentration (IC_{50}) of free DOX in NP69, 5-8F, and C666-1 cell lines (Supporting Information Fig. S3), which were subsequently used to normalize drug concentrations in subsequent experiments.

In cytotoxicity assays, S3-Lip-DOX exhibited significantly lower toxicity towards normal NP69 cells compared to free DOX. However, in NPC cells (5-8F and C666-1), the cytotoxicity of S3-Lip-DOX was comparable to that of free DOX (Fig. 2A). Similarly, EdU incorporation assays revealed that S3-Lip-DOX treatment resulted in marked inhibition of DNA synthesis in NPC cells, with minimal effect on NP69 cells (Supporting Information Fig. S4).

To investigate the mechanism of cytotoxicity, apoptosis was assessed. Flow cytometry analysis showed a significantly higher percentage of apoptotic cells in 5-8F and C666-1 populations treated with S3-Lip-DOX compared to those treated with Lip-DOX. In contrast, low levels of apoptosis were observed in NP69 cells across all treatment groups (Fig. 2B and C). Consistent with these findings, the results of Western blot analysis of

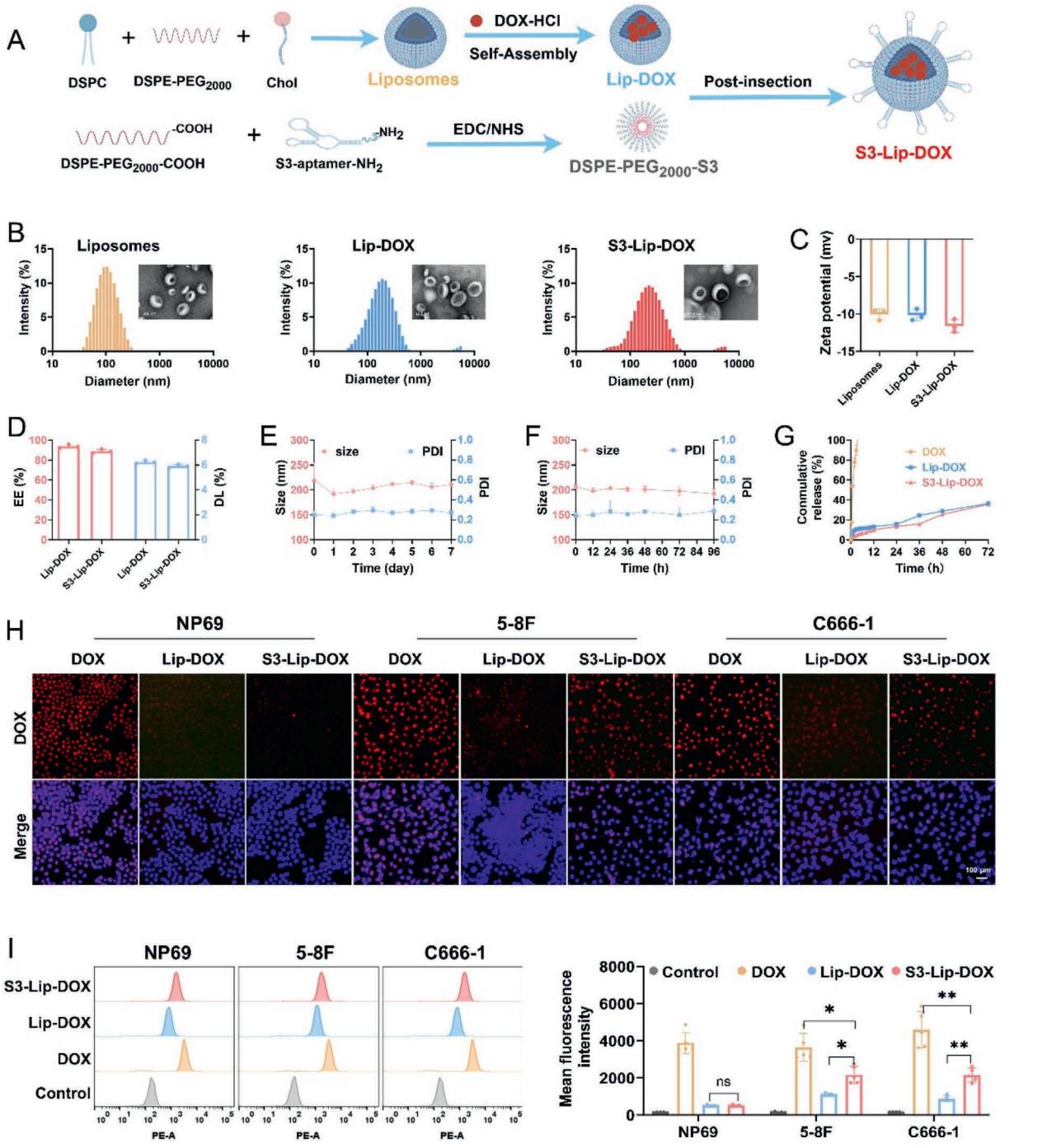

Figure 1 Preparation and characterization of S3-Lip-DOX. (A) Schematic of the S3-Lip-DOX preparation process. (B) Hydrodynamic size distribution measured by DLS and representative transmission electron microscopy (TEM) images of blank liposomes, Lip-DOX, and S3-Lip-DOX. Scale bar = 100 nm. (C) Zeta potentials of the indicated liposome formulations. (D) Encapsulation efficiency (EE) and drug loading (DL) of Lip-DOX and S3-Lip-DOX. (E) Size stability, measured by hydrodynamic size and polydispersity index (PDI), of S3-Lip-DOX stored in PBS (pH 7.4) at 4 °C over 7 days. (F) Colloidal stability (size and PDI) of S3-Lip-DOX incubated in PBS containing 10% FBS at 37 °C over 96 h. (G) *In vitro* DOX release profiles from free DOX, Lip-DOX, and S3-Lip-DOX in PBS (pH 7.4). (H) Representative fluorescence microscopy images showing cellular uptake of free DOX, Lip-DOX, or S3-Lip-DOX in various cell lines after 6 h of incubation. Scale bar = 100 μm. (I) Quantification of intracellular DOX uptake by flow cytometry after an 6 h incubation. Data in (C−G, I) are presented as mean ± SD ($n = 3$, $n = 5$ for I). Statistical significance in (I) was determined by a two-way ANOVA. ns: not significant, $^{*}P < 0.05$, $^{**}P < 0.01$.

apoptosis-related proteins demonstrated that S3-Lip-DOX treatment specifically modulated the expression of key apoptotic regulatory factors in NPC cells. Specifically, it significantly upregulated the levels of the pro-apoptotic protein Bax and the apoptotic executioner protein cleaved caspase-3, while concurrently downregulating the expression of the anti-apoptotic protein Bcl-2. Notably, none of these effects were observed in NP69 cells (Fig. 2D and E). Beyond inducing apoptosis, markers of

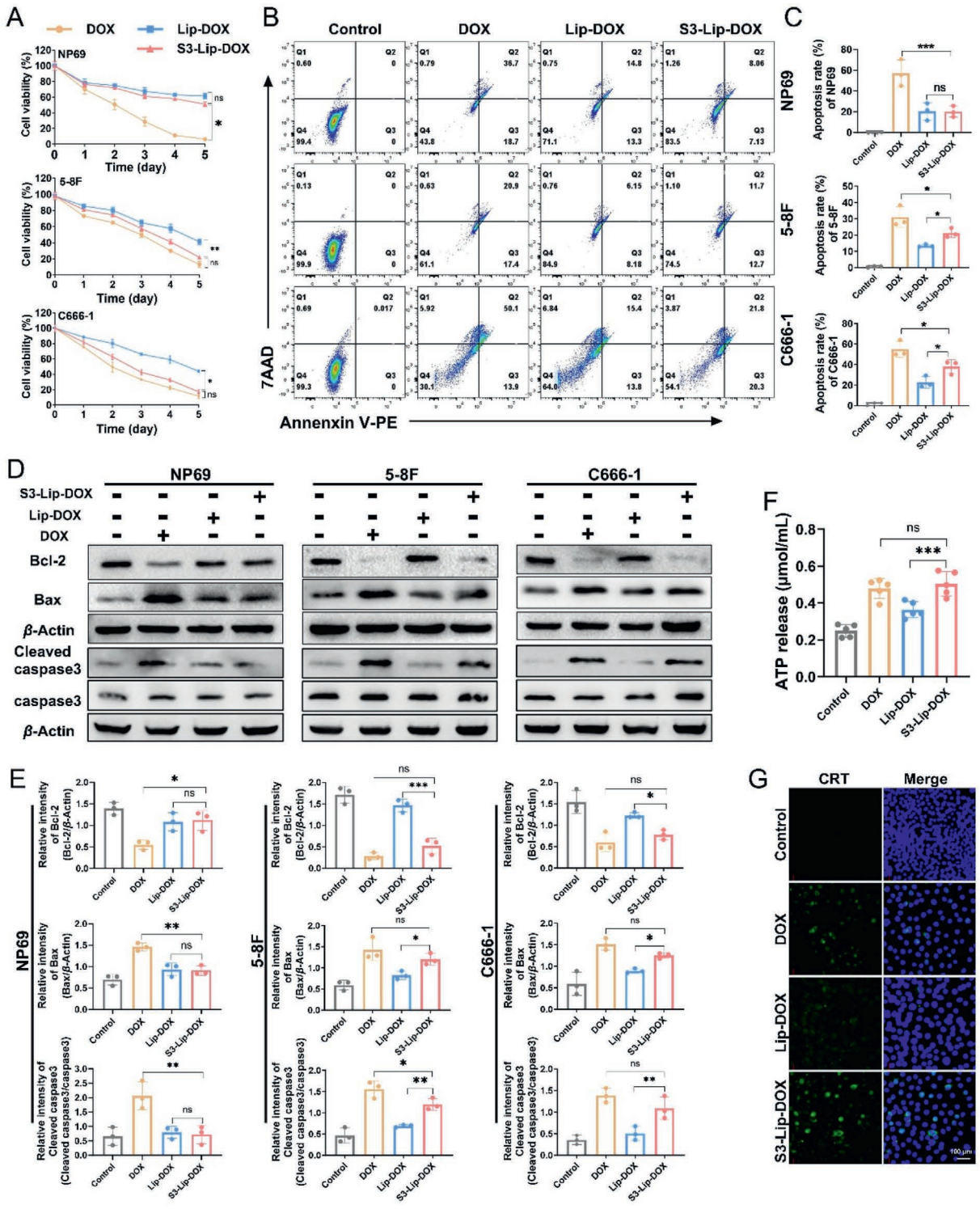

Figure 2 S3-Lip-DOX demonstrates potent anticancer efficacy and induces immunogenic cell death in NPC cells. (A) Viability of normal nasopharyngeal cells line (NP69) and NPC cell lines (5-8F, C666-1) treated with free DOX, Lip-DOX, or S3-Lip-DOX, as measured by CCK-8 assay. (B) Representative flow cytometry plots of apoptosis in NPC cells after a 48 h treatment. (C) Quantification of apoptotic (early + late) cell populations from the analysis in (B). (D) Western blot analysis of apoptosis-related proteins (Bcl-2, Bax, Cleaved caspase-3) in NPC cells following a 48 h treatment. β-Actin was used as a loading control. (E) Densitometric quantification of the protein bands shown in (D). (F) Extracellular ATP levels measured in the supernatant of 5-8F cells after a 48 h treatment. (G) Representative immunofluorescence images showing calreticulin (CRT) exposure on the surface of 5-8F cells after a 24 h treatment. Staining: CRT (green), nuclei (DAPI, blue). Scale bar = 100 μm. Data in (A, C, E, F) are presented as mean ± SD ($n = 3$; $n = 5$ for F). Statistical significance was determined by one-way ANOVA (C, E, F) or two-way ANOVA (A). *$P < 0.05$, **$P < 0.01$, ***$P < 0.001$, ****$P < 0.0001$; ns, not significant.

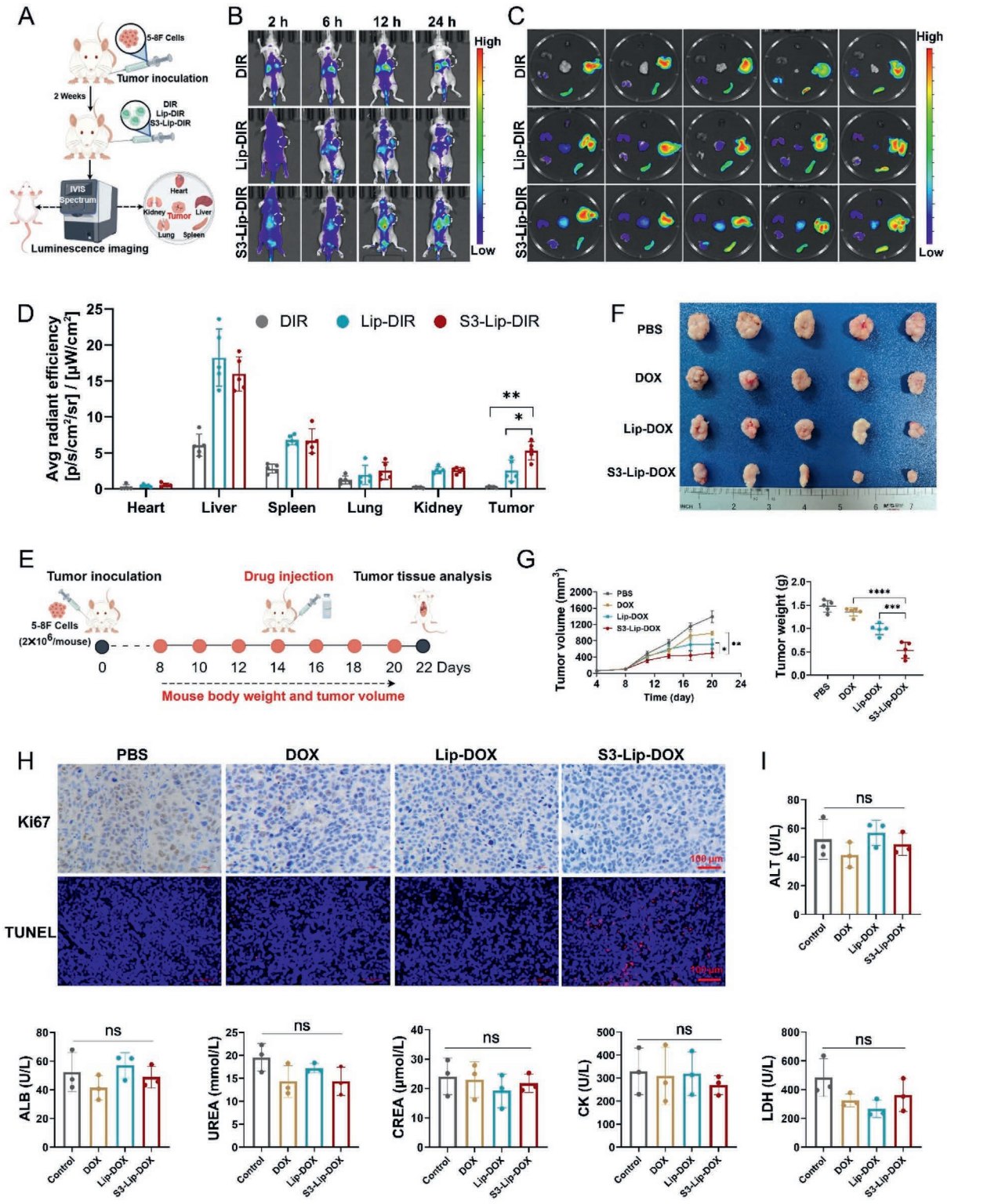

Figure 3 S3-Lip-DOX demonstrates enhanced tumor accumulation, potent *in vivo* efficacy, and a favorable safety profile. (A) Schematic of the experimental design for the *in vivo* tumor targeting and biodistribution study. (B) Representative whole-body fluorescence imaging of 5-8F tumor-bearing mice at indicated time points after intravenous injection of free DiR, Lip-DiR, or S3-Lip-DiR. (C) *Ex vivo* fluorescence images of major organs and tumors harvested 24 h post-injection. The tumor is positioned in the center of the organ array. (D) Quantification of the *ex vivo* fluorescence intensity in major organs and tumors from (C). (E) Schematic of the treatment schedule for the *in vivo* antitumor efficacy study. (F) Representative images of tumors excised from each treatment group on Day 22. (G) Tumor growth curves (left) and final tumor weights (right) of 5-8F xenograft-bearing mice after treatment. (H) Representative images of Ki67 (proliferation) and TUNEL (apoptosis) staining in tumor sections

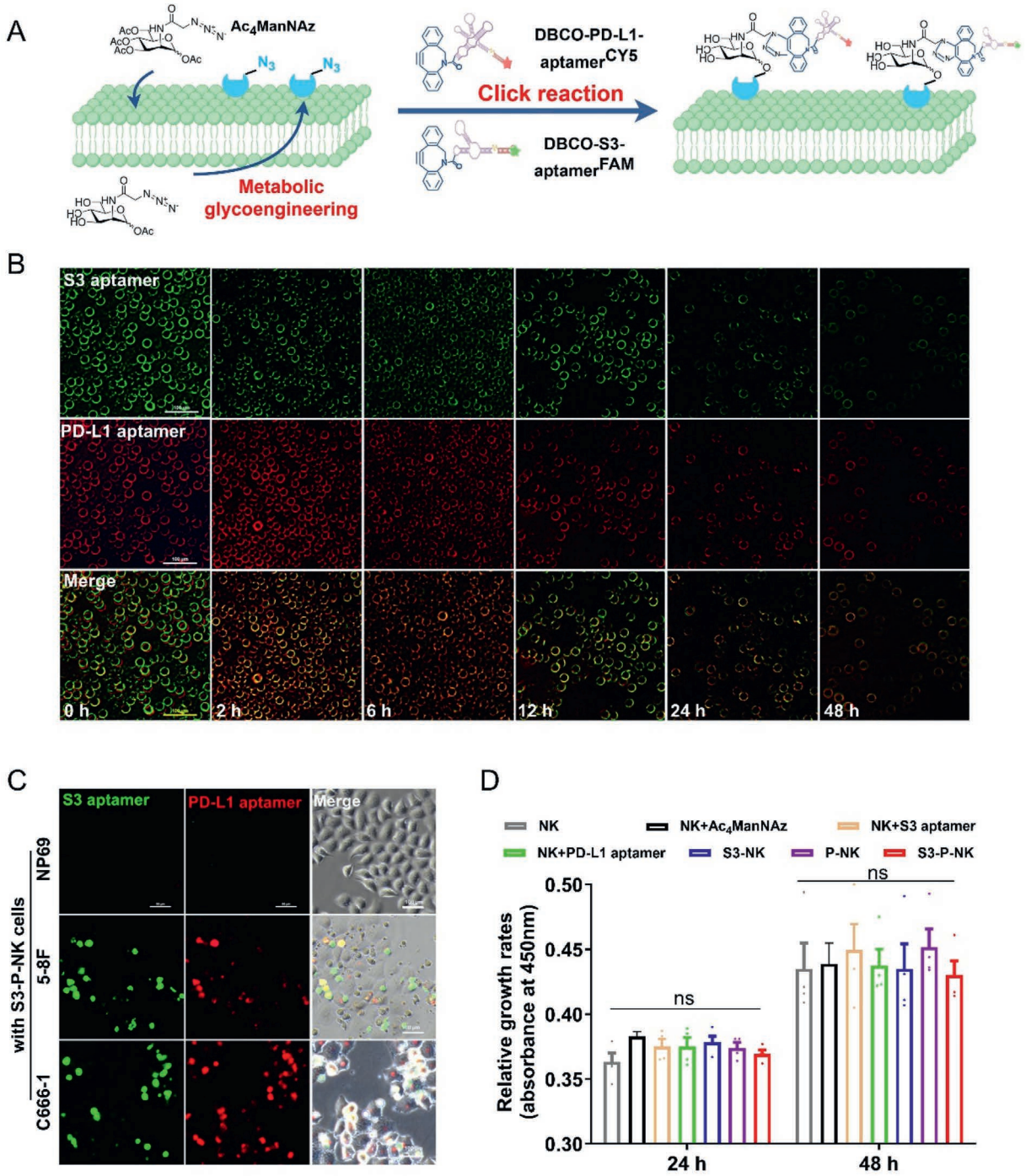

Figure 4 Preparation, characterization, and targeted binding of dual aptamer-engineered NK cells. (A) Schematic of the S3-P-NK cell preparation. The two-step process involves (1) metabolic labeling of NK-92 cell surface glycans with $Ac_4ManNAz$, followed by (2) copper-free click conjugation of DBCO-modified S3 and PD-L1 aptamers. (B) Representative fluorescence microscopy images of dual-labeled S3-P-NK cells, showing FAM-S3 aptamer (green), Cy5-PD-L1 aptamer (red), and the merged image. Scale bar = 100 μm. (C) Representative fluorescence images demonstrating the target-specific binding of S3-P-NK cells to NPC cells (5-8F, C666-1) *versus* normal nasopharyngeal cells (NP69). Cells were co-cultured at an effector-to-target (*E:T*) ratio of 10:1, and images were taken after washing to remove unbound NK cells. Scale bar = 50 μm. (D) Viability of unmodified (NK-92) and engineered (S3-P-NK) cells over 48 h, as assessed by CCK-8 assay. Data in (D) are presented as mean ± SD ($n = 4$). Statistical significance was determined by a two-way ANOVA. ns, not significant.

from each group. Scale bar = 100 μm. (I) Serum biochemical analysis for markers of liver function (ALT, ALB), kidney function (UREA, CREA), and cardiac injury (CK, LDH) from treated mice at the end of the study. Data in (D, G, I) are presented as mean ± SD ($n = 5$ for D and G; $n = 3$ for I). Statistical significance was determined by one-way ANOVA. ***$P < 0.001$, ****$P < 0.0001$; ns, not significant.

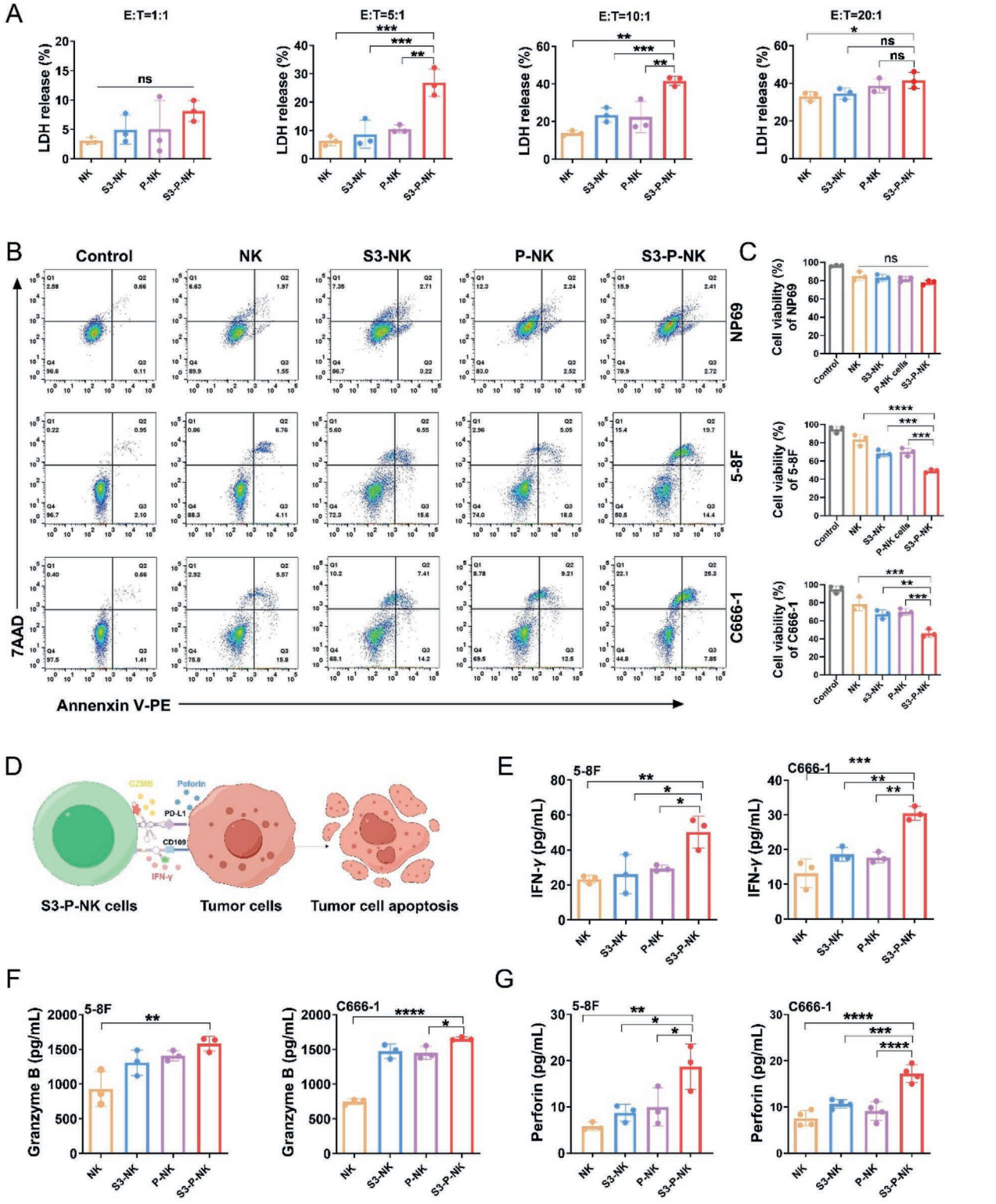

Figure 5 Aptamer-engineered NK cells exhibit enhanced targeted cytotoxicity and effector functions against NPC cells. (A) Cytotoxicity of NK, S3-NK, P-NK, and S3-P-NK cells against 5-8F target cells, measured by LDH release assay across a range of effector-to-target (E:T) ratios after a 2 h co-culture. (B) Flow cytometry images demonstrated that NP69, 5-8F, and C666-1 cells were co-cultured with NK cells at a 10:1 E:T ratio for 2 h, washed with PBS, and co-incubated for 24 h, leading to apoptosis and necrosis. (C) Quantification of total apoptotic (early + late) and necrotic cell populations from the analysis shown in (B). (D) Schematic of the proposed mechanism for S3-P-NK cell-mediated antitumor immunity, involving targeted recognition followed by the release of cytotoxic granules (perforin, granzyme B) and immunostimulatory cytokines (IFN-γ). (E−G) ELISA quantification of effector molecules released into the supernatant after co-culture of NK cells with 5-8F or C666-1 target

immunogenic cell death (ICD) were also measured. Treatment of 5-8F cells with S3-Lip-DOX led to increased extracellular ATP release and surface exposure of calreticulin (CRT). The levels of these ICD markers were comparable to those induced by free DOX and significantly greater than those observed with non-targeted Lip-DOX (Fig. 2F and G).

Collectively, these results demonstrate that S3-Lip-DOX selectively induces apoptosis and ICD in NPC cells while sparing normal epithelial cells, highlighting its dual advantages of tumor-specific cytotoxicity and immunogenic potential.

3.4. S3-Lip-DOX shows enhanced tumor accumulation, antitumor efficacy, and favorable safety profile in vivo

The *in vivo* biodistribution of DiR-labeled liposomes was monitored in NPC tumor-bearing mice. Following intravenous administration, mice treated with S3-Lip-DiR exhibited stronger fluorescence signals at the tumor site compared to those treated with non-targeted Lip-DiR or free DiR (Fig. 3A and B). *Ex vivo* imaging of harvested organs and tumors at 24 h post-injection confirmed higher fluorescence accumulation in tumors from the S3-Lip-DiR group (Fig. 3C and D).

The antitumor efficacy of S3-Lip-DOX was evaluated in a subcutaneous 5-8F xenograft model. Following the treatment schedule outlined in Fig. 3E, mice treated with S3-Lip-DOX showed significantly suppressed tumor growth compared to the PBS, free DOX, and Lip-DOX groups. The final tumor weights in the S3-Lip-DOX group were significantly lowest in all the groups (Fig. 3F and G). Immunohistochemical analysis of tumor sections from the S3-Lip-DOX group revealed a decrease in Ki-67 positive cells and an increase in TUNEL-positive cells compared to the control groups (Fig. 3H).

Systemic toxicity was evaluated throughout the study. Mice treated with S3-Lip-DOX maintained stable body weight, in contrast to the weight loss observed in the free DOX group (Supporting Information Fig. S5A). Histological analysis of major organs showed no apparent abnormalities in the S3-Lip-DOX group, whereas signs of cardiotoxicity were observed in the heart tissue of mice treated with free DOX (Fig. S5B). Serum biochemical analysis showed that markers for liver, kidney, and cardiac function remained within normal ranges for all treatment groups (Fig. 3I). Taken together, these results demonstrate that S3-Lip-DOX exhibits precise tumor targeting, potent antitumor activity, and low systemic toxicity *in vivo*, underscoring its translational potential for the targeted treatment of NPC.

3.5. Preparation and characterization of dual-aptamer engineered NK cells (S3-P-NK)

To construct a dual-targeting cellular therapeutic, we employed a two-step bio-orthogonal chemistry approach to conjugate both S3 and PD-L1 aptamers onto the NK-92 cell surface, generating S3-P-NK cells (Fig. 4A). Fluorescence microscopy confirmed the successful and stable co-localization of both FAM-S3 (green) and Cy5-PD-L1 (red) aptamers on the cell membrane for at least 48 h (Fig. 4B).

We next assessed the functional consequences of this engineering. Co-culture binding assays revealed that S3-P-NK cells efficiently and specifically bound to NPC cell lines (5-8F and C666-1), whereas minimal adhesion was observed with normal nasopharyngeal NP69 cells, confirming the high specificity of the targeting strategy (Fig. 4C). To unequivocally demonstrate the advantage of the dual-aptamer design, we compared the binding efficacy of S3-P-NK cells against that of single-aptamer engineered cells (S3-NK and P-NK). Crucially, S3-P-NK cells exhibited significantly enhanced binding to 5-8F NPC cells compared to both single-targeted controls, highlighting a synergistic effect of dual engagement (Supporting Information Fig. S6). Furthermore, the entire engineering process proved to be highly biocompatible, as the viability of S3-P-NK cells remained comparable to that of unmodified NK-92 cells (Fig. 4D, Supporting Information Fig. S7A and S7B).

Collectively, these results demonstrate that our dual-aptamer engineering strategy successfully endows NK cells with potent and specific NPC-targeting capabilities, which are demonstrably superior to single-targeting approaches, all while maintaining excellent biocompatibility.

3.6. Dual-aptamer engineering potentiates specific cytotoxicity by enhancing NK cell effector functions

To determine if this enhanced targeting translated into superior function, we first assessed the cytotoxic potential of our engineered cells. An LDH release assay revealed that S3-P-NK cells induced markedly superior lysis of 5-8F target cells, significantly outperforming parental NK-92 cells and both single-aptamer controls (S3-NK and P-NK) at key *E:T* ratios of 5:1 and 10:1 (Fig. 5A). This result provides the first functional evidence of a synergistic anti-tumor effect.

Flow cytometry analysis confirmed that this superior cytotoxicity was driven by the induction of apoptosis. In both 5-8F and C666-1 cancer cell lines, S3-P-NK cells induced a percentage of apoptotic and necrotic cells that was significantly higher than all control groups: parental NK, S3-NK, and P-NK. Underscoring the therapy's precision, this potent effect was highly specific to cancer cells, as viability in normal NP69 cells remained unaffected, confirming a favorable safety profile (Fig. 5B and C).

To elucidate the molecular mechanism driving this functional superiority, we investigated the activation of the NK cell effector pathway, as illustrated in Fig. 5D. Indeed, upon co-incubation with NPC cells, S3-P-NK cells unleashed a significantly more potent effector response, secreting levels of the immunostimulatory cytokine IFN-γ and the cytotoxic proteins granzyme B (GZMB) and perforin that were substantially higher than those released by parental NK cells or either single-aptamer control (Fig. 5E−G). This finding directly links the dual-aptamer design to enhanced cellular activation.

Taken together, these data paint a clear and consistent picture: the dual-aptamer strategy creates a powerful synergistic effect by translating superior target recognition into a more robust activation of the NK cell's intrinsic cytotoxic machinery. This culminates in a potent, specific, and enhanced anti-tumor response that

cells (E:T = 10:1) for 2 h, PBS washing, and co-incubation for 24 h: (E) IFN-γ, (F) Granzyme B, (G) Perforin. Data in (A, C, E, F, G) are presented as mean ± SD ($n = 3$). Statistical significance was determined by one-way ANOVA. *$P < 0.05$, **$P < 0.01$, ***$P < 0.001$, ****$P < 0.0001$; ns, not significant.

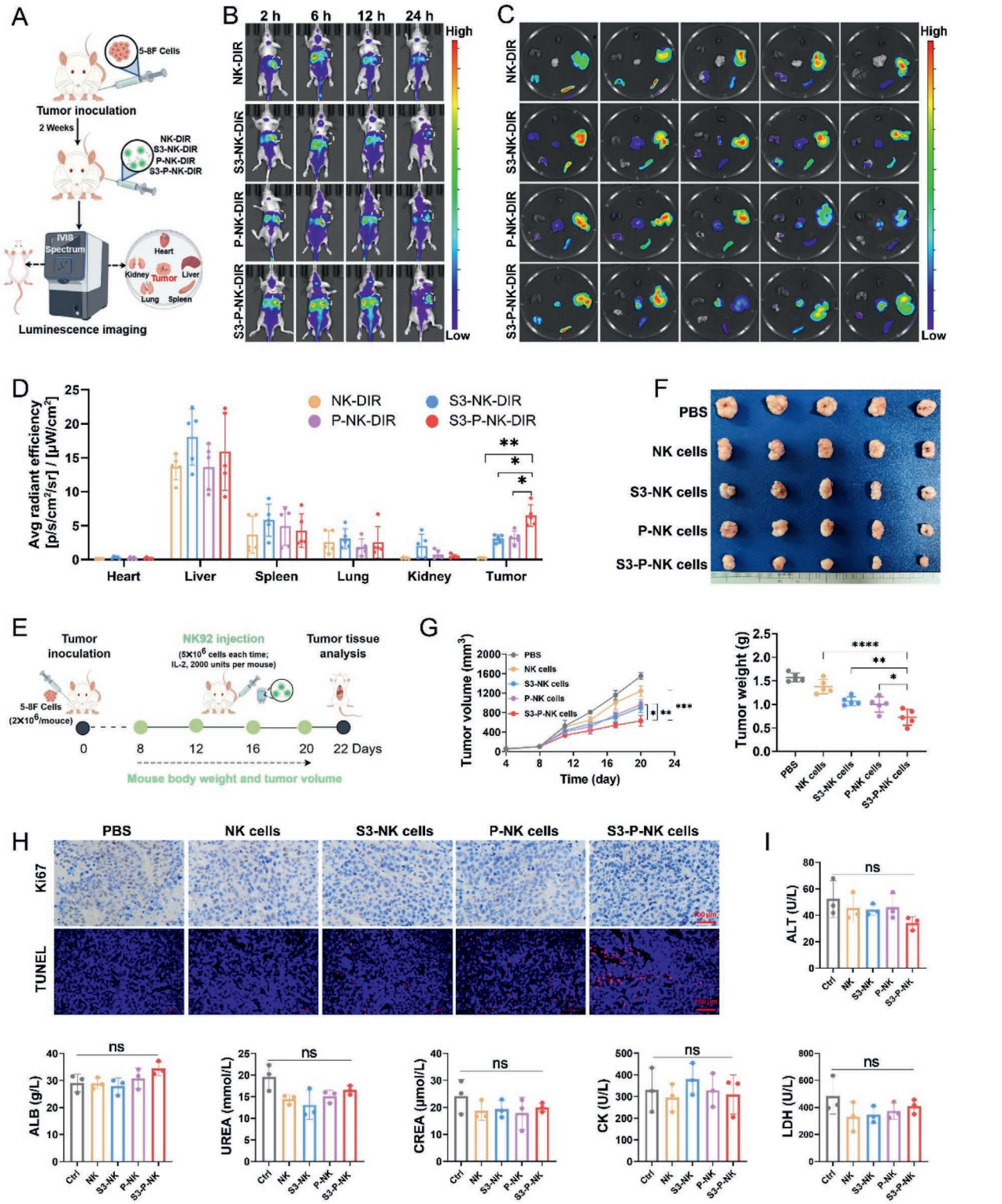

Figure 6 S3-P-NK cells exhibit superior tumor-homing, potent antitumor efficacy, and systemic safety *in vivo*. (A) Schematic of the experimental design for the *in vivo* biodistribution study. (B) Representative whole-body near-infrared fluorescence imaging of 5-8F tumor-bearing mice at indicated time points after intravenous injection of various DiR-labeled NK cell groups. (C) *Ex vivo* fluorescence images of major organs and tumors harvested 24 h post-injection. The tumor is positioned in the center of the organ array. (D) Quantification of the *ex vivo* fluorescence intensity in major organs and tumors from (C). (E) Schematic of the treatment schedule for the *in vivo* antitumor efficacy study. (F) Representative images of tumors excised from each treatment group at the study endpoint on Day 22. (G) Tumor growth curves (left) and final tumor weights (right) of 5-8F xenograft-bearing mice following the indicated treatments. (H) Representative images of Ki67 (proliferation) and TUNEL (apoptosis) staining in tumor sections from each group. Scale bar = 100 μm. (I) Serum biochemical analysis for markers of liver function

is demonstrably superior to that achieved by single-aptamer modifications alone.

3.7. S3-P-NK cells exhibit enhanced tumor homing and antitumor efficacy in vivo

To translate our promising *in vitro* findings into a therapeutically relevant context, we first assessed whether dual-aptamer engineering could improve the tumor-homing capacity of NK cells *in vivo*. Using a near-infrared fluorescence imaging system in NPC-bearing mice, we observed that S3-P-NK cells demonstrated vastly superior localization to the tumor site 24 h post-injection, significantly outperforming the parental NK and single-aptamer control groups (Fig. 6A and B). This superior targeting was quantitatively confirmed by *ex vivo* analysis of harvested organs, which showed the highest fluorescence intensity concentrated within the tumor tissues of the S3-P-NK group (Fig. 6C and D). While some signal was expectedly observed in the liver and spleen, the data clearly indicate that the dual-aptamer design effectively enhances the specific accumulation of NK cells at the tumor.

Having confirmed superior tumor homing, we next investigated whether this translated to enhanced therapeutic efficacy. In a 22-day study, mice treated with S3-P-NK cells exhibited the most profound tumor growth inhibition, resulting in significantly smaller tumor volumes and lower final tumor weights compared to the PBS control and all other NK cell treatment groups (Fig. 6E−G). This macroscopic tumor control was underpinned by changes at the cellular level; histological analysis revealed that tumors from the S3-P-NK group had a marked decrease in the proliferation marker Ki-67 and a significant increase in apoptotic TUNEL-positive cells, confirming a powerful localized anti-tumor effect (Fig. 6H).

Crucially, this potent antitumor efficacy was achieved without inducing systemic toxicity. Throughout the treatment regimen, we rigorously monitored for adverse effects. Comprehensive blood biochemical analyses confirmed that markers for liver, kidney, and cardiac function remained within normal physiological ranges across all groups (Fig. 6I). Furthermore, no significant changes in body weight or evidence of histopathological damage to major organs were observed (Fig. S7A and 7B). Together, these *in vivo* results demonstrate that S3-P-NK cells are a potent and safe therapeutic agent, capable of superior tumor homing that translates directly into robust and specific tumor eradication.

3.8. A synergistic triple-combination therapy maximizes in vitro cytotoxicity

To construct the most potent therapeutic regimen, we first aimed to identify the optimal antibody partner for our S3-P-NK cells, focusing on leveraging Antibody-Dependent Cell-Mediated Cytotoxicity (ADCC). We compared three anti-PD-L1 antibodies with varying ADCC capabilities: Atezolizumab (ADCC-null), Avelumab (wild-type ADCC), and an engineered Atezolizumab/IgG1 (ADCC-enhanced). When combined with S3-P-NK cells, the ADCC-enhanced Atezolizumab/IgG1 dramatically outperformed the other antibodies, yielding significantly greater tumor cell lysis and growth inhibition (Fig. 7A and B). Heat map and live cell imaging analyses clearly demonstrated that the synergistic effect was dependent on both dose and time, with the optimal cytotoxic effect observed at an effector-to-target ratio of 5:1 and a concentration of 20 μg/mL of Atezolizumab (IgG1 type) (Fig. 7C−E). These findings indicate that Atezolizumab is a suitable antibody for the current combination strategy.

Next, we hypothesized that our targeted chemotherapy, S3-Lip-DOX, could further enhance this efficacy by sensitizing tumor cells to the antibody-NK cell attack. We investigated how S3-Lip-DOX treatment affected the expression of PD-L1, the target of Atezolizumab/IgG1. As confirmed by flow cytometry, S3-Lip-DOX treatment resulted in a significant upregulation of PD-L1 expression on the surface of NPC cells, reaching approximately 4-fold higher than the control group (Fig. 7F). This crucial finding suggests a dual benefit of the chemotherapy: not only does it exert direct cytotoxicity, but it also renders surviving cancer cells more susceptible to ADCC by increasing the density of the target antigen.

Based on these synergistic findings, we tested the ultimate triple-combination therapy: S3-Lip-DOX, Atezolizumab/IgG1, and S3-P-NK cells. This three-pronged attack resulted in a near-complete eradication of cancer cells, reducing viability to just $10.58 \pm 1.43\%$ and driving LDH release to $66.07 \pm 5.74\%$ after 48 h. As hypothesized, this outcome was profoundly more effective than any monotherapy or dual-combination therapy tested, demonstrating a powerful and multi-faceted synergistic effect (Fig. 7G).

3.9. Triple-combination therapy suppresses tumor growth and remodels the innate immune microenvironment in vivo

To validate the synergistic potential of our triple-combination strategy *in vivo*, we utilized an NPC xenograft model. Following the treatment schedule detailed in Fig. 8A, we observed that the triple-combination regimen (G6) produced profound antitumor efficacy. This group exhibited the greatest inhibition of tumor growth, with final tumor weights being significantly lower than those in the PBS control group (G1, $P < 0.0001$) and all other monotherapy or dual-therapy arms (G2−G5) (Fig. 8B−D). This result provides definitive *in vivo* evidence for the powerful synergy between the targeted chemotherapy, ADCC-enhanced antibody, and dual-aptamer engineered NK cells.

To elucidate the cellular mechanisms driving this superior efficacy, we analyzed the tumor immune microenvironment. Flow cytometry revealed a dramatic remodeling of innate immune populations (Fig. 8E, Supporting Information Fig. S9A and S9B). The proportion of pro-inflammatory $CD86^+$ macrophages in the triple-therapy group (G6) surged to 30.9%, a stark and statistically significant increase compared to the 21.2% in the PBS control group (G1) ($P < 0.0001$) and all other treatment arms. Similarly, mature dendritic cells ($CD11c^+MHCII^+CD86^+$) reached 28.5% in the G6 group, a significant leap from 14.8% in the control ($P < 0.0001$) and substantially higher than all other cohorts (Fig. 8F).

(ALT, ALB), kidney function (UREA, CREA), and cardiac injury (CK, LDH) from treated mice at the end of the study. Data in (D, G, I) are presented as mean ± SD ($n = 5$ for D, G; $n = 3$ for I). Statistical significance was determined by one-way ANOVA. $^*P < 0.05$, $^{**}P < 0.01$, $^{****}P < 0.0001$; ns, not significant.

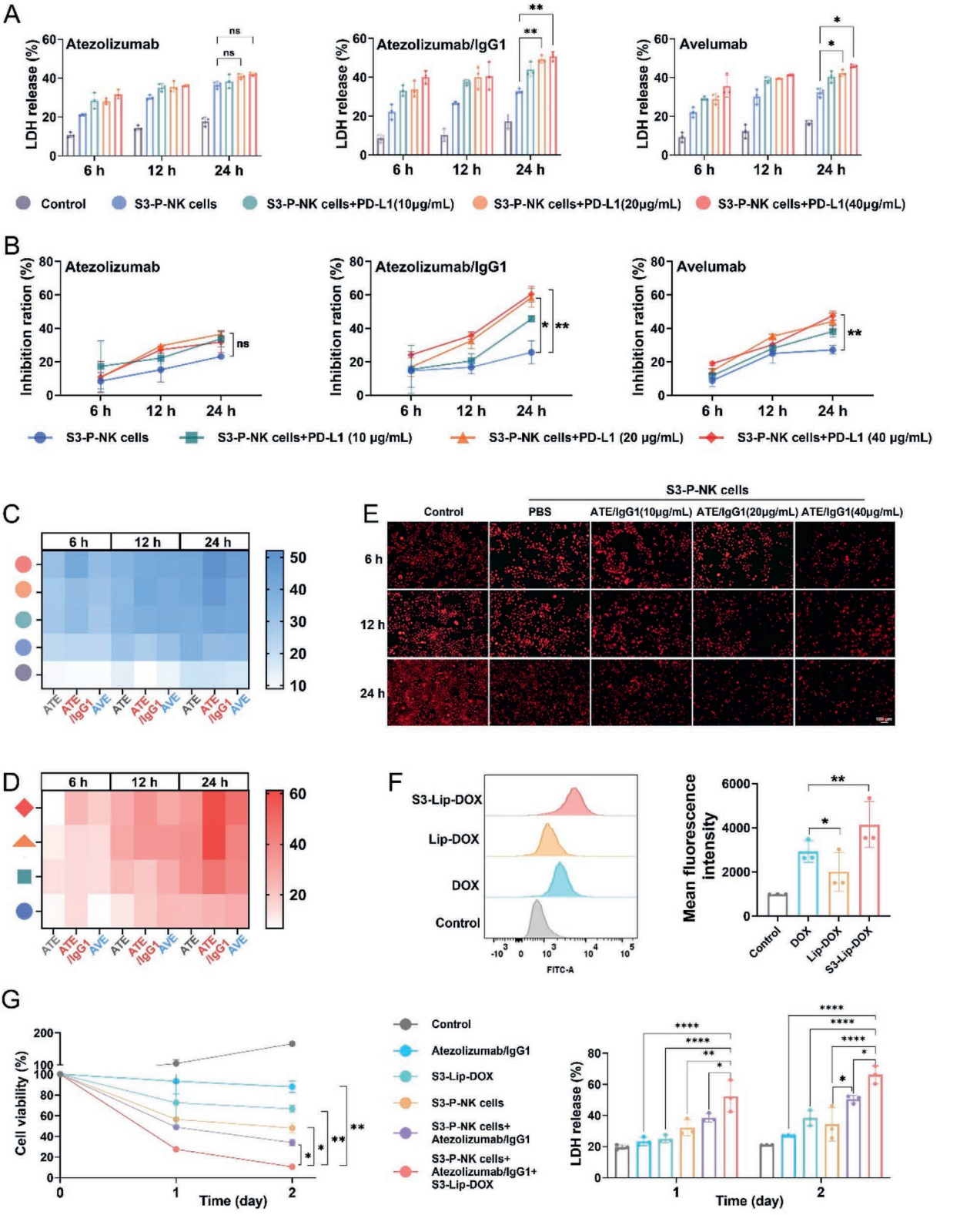

Figure 7 S3-Lip-DOX sensitizes NPC cells to a synergistic triple-combination therapy involving S3-P-NK cells and PD-L1 blockade. (A, B) Cytotoxicity and viability of 5-8F cells after co-culture with S3-P-NK cells (*E:T* ratio = 5:1) and increasing concentrations of PD-L1 antibodies (Atezolizumab, Atezolizumab/IgG1, and Avelumab). Efficacy was measured by (A) LDH release and (B) CCK-8 assay. (C, D) Synergy analysis of the S3-P-NK and PD-L1 antibody combinations, visualized as heatmaps for (C) cytotoxicity (LDH release) and (D) cell viability (CCK-8). (E) Representative time-lapse microscopy images tracking the interaction between S3-P-NK cells and CM-DiI-labeled 5-8F cells (red) in the presence of Atezolizumab/IgG1. Scale bar = 50 μm. (F) PD-L1 surface expression on 5-8F cells after S3-Lip-DOX treatment, analyzed by flow cytometry.

Multiplex immunofluorescence (mIF) staining not only validated these findings but also provided crucial spatial context within the tumor architecture (Fig. 8G and Supporting Information Fig. S10): 1. Tumor cell state: Consistent with the tumor growth data, the G6 group showed a decisive shift toward cell death, evidenced by a dramatic decrease in the proliferative $Ki67^+$ area and a significant increase in the apoptotic $TUNEL^+$ area compared to all other groups ($P < 0.001$ or $P < 0.0001$) (Fig. 8H). 2. Macrophage polarization: The therapy effectively reprogrammed the macrophage landscape. The area of pro-inflammatory M1-like ($CD86^+$) macrophages expanded to approximately 10% in the G6 group, significantly greater than all other groups ($P < 0.01$ or $P < 0.0001$). Concurrently, the area of immunosuppressive M2-like ($CD206^+$) macrophages was significantly reduced in all active treatment groups (G3−G6) compared to the PBS control ($P < 0.001$) (Fig. 8I). 3. Dendritic cell maturation: Corroborating the flow cytometry data, the G6 cohort displayed the largest area of mature, CD86-expressing dendritic cells, reaching approximately 9%. This represented a significant increase over all other treatment groups ($P < 0.05$, $P < 0.01$, or $P < 0.001$) (Fig. 8J).

In summary, our *in vivo* data demonstrate that the triple-combination therapy achieves superior tumor suppression by mechanistically linking direct cytotoxicity with a comprehensive and favorable remodeling of the tumor microenvironment. This is characterized by enhanced apoptosis, a robust polarization of macrophages towards a pro-inflammatory M1 phenotype, and a significant increase in the maturation of antigen-presenting dendritic cells.

4. Discussion

Nasopharyngeal carcinoma (NPC) presents a formidable therapeutic challenge, particularly in its recurrent or metastatic forms, where conventional treatments often fail. The intricate and often immunosuppressive tumor microenvironment (TME) of NPC necessitates innovative strategies that can overcome tumor resistance and effectively engage the immune system[34-36]. Notably, multi-component strategies that synergistically target distinct biological pathways are emerging as a powerful paradigm for overcoming the complexity and adaptability of diseases like cancer and viral infections[37-39]. In this study, we designed and validated a multi-component, synergistic therapeutic strategy that combines targeted chemotherapy, dual-aptamer-engineered NK cells, and an ADCC-enhanced anti-PD-L1 antibody. Our collective findings demonstrate that this triple-combination therapy not only potently suppresses tumor growth but does so by fundamentally reprogramming the innate immune landscape, transforming it from a suppressive to a pro-inflammatory state.

Our strategy was built upon a rational, stepwise design, with each component addressing a specific barrier to effective therapy. The first element, S3-Lip-DOX, was engineered to solve the problem of the off-target toxicity. By leveraging the S3 aptamer to target CD109, which our data had previously confirmed is highly expressed on NPC cells[13], we achieved precise drug delivery and enhanced tumor cell killing *in vivo*, with a favorable safety profile. Critically, we discovered that this targeted chemotherapy induced a significant upregulation of PD-L1 on tumor cells. This finding is a cornerstone of our synergistic model; the chemotherapy does not merely kill tumor cells but actively "paints a target" on the survivors. In essence, by inducing immunogenic cell death (ICD) and releasing a host of tumor antigens, S3-Lip-DOX effectively transforms the tumor into an *in situ* vaccine, providing the antigenic fuel for a subsequent, broader immune attack[40-43].

The second pillar of our approach was the development of S3-P-NK cells, designed to overcome the notorious challenge of poor tumor homing that has limited the efficacy of adoptive NK cell therapies[18,44,45]. By equipping NK cells with two distinct aptamers—S3 for CD109 and P for PD-L1—we created a "dual-guidance" system. Our *in vivo* biodistribution studies unequivocally demonstrated that these S3-P-NK cells exhibited vastly superior tumor accumulation compared to unmodified or single-aptamer-modified cells. This enhanced targeting translated directly into superior tumor suppression. Moreover, our choice of the NK-92 cell line as the engineering chassis represents a scalable, "off-the-shelf" therapeutic strategy. This stands in stark contrast to autologous cell therapies like CAR-T, which are patient-specific, costly, and time-consuming to manufacture, thereby offering a pathway to a more accessible and economically viable cell-based medicine[46-49].

Perhaps the most critical insight from this study is the redefinition of the anti-PD-L1 antibody's role in the initial phase of immunotherapy. Conventionally viewed as a "T-cell guardian" that functions late in the immune cycle to prevent T-cell exhaustion, our work reveals its potent, immediate function as an "innate immune potentiator." In our T-cell-deficient model, the Atezolizumab/IgG1, engineered to restore ADCC, acted as a molecular bridge, converting the immunosuppressive PD-L1 signal into a "death tag" for potent destruction by our NK cells [27,50-52]. This was directly validated by our *in vivo* data, where the combination of S3-P-NK cells and the ADCC-enhanced antibody was significantly more effective than NK cells alone. This highlights that such antibodies can play a vital role on the "first line" of immune defense, not just the last.

The true power of this strategy was revealed when all three components were combined *in vivo*. The profound tumor suppression observed was not merely additive but was driven by a synergistic reprogramming of the innate immune TME. The initial dual assault from the S3-Lip-DOX-driven *in situ* vaccination and S3-P-NK cell killing created a powerful stimulus of extensive tumor cell apoptosis, as evidenced by the surge in $TUNEL^+$ cells. This wave of cell death releases a cascade of tumor antigens and danger-associated molecular patterns (DAMPs)[53,54] Our multiplex immunofluorescence data vividly illustrated the consequences: a functional switch of macrophages from an immunosuppressive M2 phenotype to a pro-inflammatory, phagocytic M1 state, and the maturation of dendritic cells into professional antigen-presenting cells (APCs). This inversion of the M1/M2 ratio and the activation of DCs are the hallmarks of an inflamed TME, transforming it from "cold" to "hot" and ready to orchestrate a broader anti-tumor response[55-58].

We must objectively acknowledge the primary limitation of this study—the use of an immunodeficient mouse model. This approach was necessitated by the lack of murine NPC cell lines, which makes

(G) Efficacy of the triple-combination therapy (S3-P-NK + Atezolizumab/IgG1 + S3-Lip-DOX) against 5-8F cells, assessed by CCK-8 viability (left) and LDH cytotoxicity (right) assays. Data are presented as mean ± SD ($n = 3$ for A, B, G; $n = 4$ for E, F). Statistical significance was determined by two-way ANOVA (A, B, G) or one-way ANOVA (E, F). *$P < 0.05$, **$P < 0.01$, ****$P < 0.0001$.

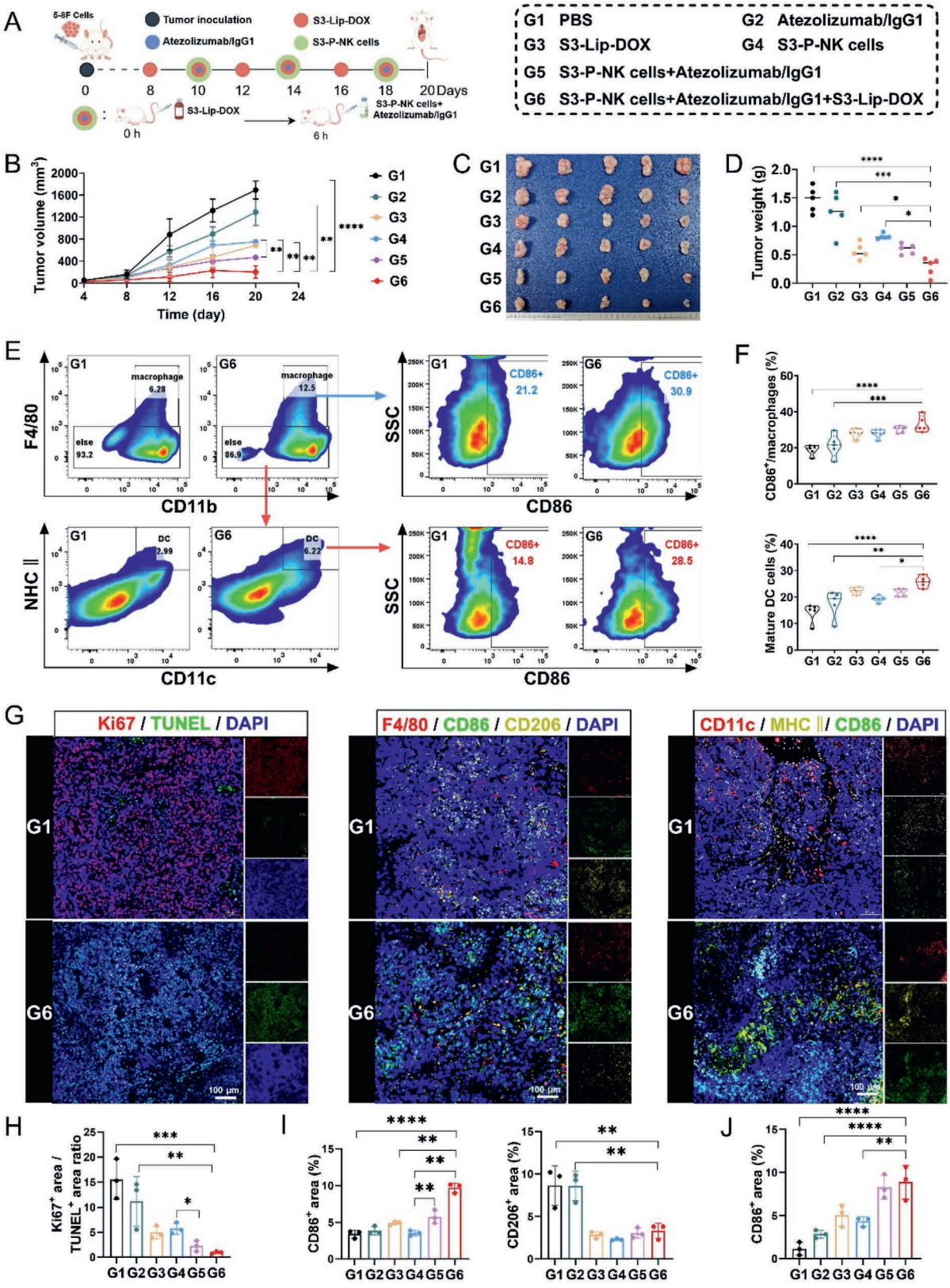

Figure 8 Triple-combination therapy demonstrates potent synergistic antitumor efficacy and favorably remodels the tumor immune microenvironment *in vivo*. (A) Schematic of the *in vivo* triple-combination therapy schedule, detailing the doses, administration routes, and timing for S3-Lip-DOX, Atezolizumab/IgG1, and S3-P-NK cells. (B) Tumor growth curves monitored *in vivo* following different treatments. (C) Representative images of tumors excised from all treatment groups at the study endpoint on Day 22. (D) Final tumor weights quantified from each treatment group at the end of the study. (E) Representative flow cytometry plots showing the infiltration of activated macrophages

human tumor xenografts the established standard for *in vivo* evaluation[59-61]. However, this immunodeficient setting was also a strategic choice, providing an unambiguous platform to dissect the synergy of our tripartite strategy and correctly interpret the resulting *in vivo* efficacy. Specifically, it allowed us to demonstrate a clear "Pretreatment-Attack-Amplify" cascade: chemotherapy first upregulates PD-L1 on tumor cells, which then serves as a fresh target for the dual-targeted NK cells, and this entire process is massively amplified by the targeted Atezolizumab/IgG1 antibody through potent ADCC activity. The T-cell-free environment was essential to unequivocally prove that this powerful synergy is rooted in innate immunity. Having established this potent, T-cell-independent killing paradigm, it is reasonable to propose that in an immunocompetent host, it would serve as the initial spark for a much broader anti-tumor response. The initial innate immune activation and antigen release would lead to APC maturation and migration, priming a powerful, tumor-specific T-cell response. In such a scenario, the Atezolizumab/IgG1 antibody would unleash a dual-pronged attack: it would not only continue to drive the initial innate immune killing *via* ADCC, but would also perform its canonical checkpoint blockade function, sustaining the newly generated T-cell response by blocking the PD-1/PD-L1 axis[62-64]. This creates a self-amplifying feedback loop, yet validating this compelling hypothesis is challenging. The limitations of current humanized mouse models in recapitulating the EBV-driven NPC microenvironment underscore a critical predicament for the field. Therefore, our work not only validates a highly effective synergistic therapeutic strategy but also highlights the urgent need for more sophisticated models to fully harness and translate such complex, multi-stage immunotherapies.

5. Conclusions

Overall, this study presents a rationally designed, triple-combination therapeutic strategy that effectively overcomes key barriers in NPC treatment. We have demonstrated that combining targeted chemotherapy, dual-aptamer-guided "off-the-shelf" NK cells, and an ADCC-enhanced antibody creates a powerful synergy that not only eradicates established tumors but also fundamentally remodels the tumor microenvironment. By redefining the immediate role of a PD-L1 antibody to potentiate innate killing, our work provides a compelling blueprint for creating a robust, closed-loop anti-tumor immune response, offering significant translational potential for NPC and other immunologically challenging solid tumors.

Acknowledgments

This work was supported by the National Natural Science Foundation of China (Nos. 82204262, 81773179, and 2204262, China), the Key Research and Development Program of Hunan (No. 2022SK2055, China), the Natural Science Foundation of Hunan Province (Nos. 2020JJ4771 and 2023JJ30733, China). The schematic illustration of the graphical abstract was drawn by Figdraw (https://www.figdraw.com).

Author contributions

Chaoyan Yao: Methodology, Data curation, Writing-original draft. Lei Wang: Visualization, Data curation. Weidong Liu: Formal analysis, Methodology. Ning Shi: Formal analysis, Drawing schematic illustration. Ziling Liao: Investigation. Yuxuan Fu: Formal analysis, Investigation. Jinhao Ouyang:Methodology. Xuan Lei: Data curation. Qianping Huang: Formal analysis. Siyu Li: Data curation. Yihua Zhouyang: Writing-review & editing. Pinnan Zhao: Project administration, Software. Jie Wang: Project administration, Software. Hongjuan Xu: Methodology. Wenhu Zhou: Methodology, Conceptualization. Xingjun Jiang: Conceptualization, Supervision. Xiang Gao: Visualization, Supervision. Caiping Ren: Conceptualization, Resources, Funding acquisition, Supervision. Longlong Luo: Conceptualization, Methodology, Writing−review & editing, Supervision. All of the authors have read and approved the final manuscript.

Conflicts of interest

The authors have no conflicts of interest to declare.

Appendix A. Supporting information

Supporting information to this article can be found online at https://doi.org/10.1016/j.apsb.2025.10.007.

References

1. Chen YP, Chan ATC, Le QT, Blanchard P, Sun Y, Ma J. Nasopharyngeal carcinoma. *Lancet* 2019;**394**:64−80.
2. Cui MM, Cheng HJ, Yuan LL, Zhang M, Chen JY, Jia JJ, et al. Burden of nasopharyngeal carcinoma in Asia from 1990 to 2021. *J Dent* 2025;**154**:105583.
3. Box VG. The intercalation of DNA double helices with doxorubicin and nogalamycin. *J Mol Graph Model* 2007;**26**:14−9.
4. Qiao XH, van der Zanden SY, Wander DPA, Borràs DM, Song JY, Li XY, et al. Uncoupling DNA damage from chromatin damage to detoxify doxorubicin. *Proc Natl Acad Sci U S A* 2020;**117**:15182−92.
5. Lu CX, Wei JW, Gao C, Sun ML, Dong D, Mu ZY. Molecular signaling pathways in doxorubicin-induced nephrotoxicity and potential therapeutic agents. *Int Immunopharmacol* 2025;**144**:113373.
6. Roomi MW, Kalinovsky T, Roomi NW, Rath M, Niedzwiecki A. Prevention of adriamycin-induced hepatic and renal toxicity in male BALB/c mice by a nutrient mixture. *Exp Ther Med* 2014;**7**:1040−4.
7. Zhou YJ, Ge QQ, Wang X, Wang YH, Sun QQ, Wang JH, et al. Advances in lipid nanoparticle-based disease treatment. *ChemMedChem* 2025;**20**:e202400938.

(F4/80$^+$CD11b$^+$CD86$^+$) and mature dendritic cells (CD11c$^+$MHCII$^+$CD86$^+$) within the tumor microenvironment of treated mice. (F) Quantification of the percentage of activated macrophages and mature dendritic cells from the flow cytometry analysis shown in (E). (G) Representative multiplex immunofluorescence images of tumor sections from key treatment groups. Panels show tumor cell proliferation (Ki67, red), apoptosis (TUNEL, green), macrophage polarization (F4/80, red; CD86, green; CD206, yellow), and dendritic cell maturation (CD11c, red; MHC II, yellow; CD86, green). Nuclei are counterstained with DAPI (blue). Scale bar = 100 μm. (H−J) Quantitative analysis of positive signal area in multiplex immunofluorescence images (G, S10): Ki67$^+$ area/TUNEL$^+$ area ratio (H); CD86$^+$ area (M1 macrophages) and CD206$^+$ area (M2 macrophages) (I); CD86$^+$ area (dendritic cells, DCs) (J). Data in (B, D, F, H−J) are presented as mean ± SD ($n = 5$). Statistical significance was determined by one-way ANOVA (D, F, H−J) or two-way ANOVA (B). *$P < 0.05$, **$P < 0.01$, ***$P < 0.001$, ****$P < 0.0001$.

8. Agrawal SS, Baliga V, Londhe VY. Liposomal formulations: a recent update. *Pharmaceutics* 2024;**17**:36.
9. Allahou LW, Madani SY, Seifalian A. Investigating the application of liposomes as drug delivery systems for the diagnosis and treatment of cancer. *Int J Biomater* 2021;**2021**:3041969.
10. Zi YX, Yang KY, He JH, Wu ZM, Liu JP, Zhang WL. Strategies to enhance drug delivery to solid tumors by harnessing the EPR effects and alternative targeting mechanisms. *Adv Drug Deliv Rev* 2022;**188**: 114449.
11. Jain RK, Stylianopoulos T. Delivering nanomedicine to solid tumors. *Nat Rev Clin Oncol* 2010;**7**:653−64.
12. Minchinton AI, Tannock IF. Drug penetration in solid tumours. *Nat Rev Cancer* 2006;**6**:583−92.
13. Jia WT, Ren CP, Wang L, Zhu B, Jia W, Gao MH, et al. CD109 is identified as a potential nasopharyngeal carcinoma biomarker using aptamer selected by cell-SELEX. *Oncotarget* 2016;**7**:55328−42.
14. Liu XW, Jiang BC, Cheng AL, Guo YW, Wang L, Liu WD, et al. The effects of doxorubicin loaded aptamer S3-linked DNA tetrahedrons on nasopharyngeal carcinoma. *J Otolaryngol Head Neck Surg* 2023;**52**:79.
15. Childs RW, Carlsten M. Therapeutic approaches to enhance natural killer cell cytotoxicity against cancer: the force awakens. *Nat Rev Drug Discov* 2015;**14**:487−98.
16. Fang F, Xiao WH, Tian ZG. NK cell-based immunotherapy for cancer. *Semin Immunol* 2017;**31**:37−54.
17. Du NW, Guo FF, Wang YF, Cui JW. NK cell therapy: a rising star in cancer treatment. *Cancers (Basel)* 2021;**13**:4129.
18. Lian GY, Mak TS, Yu XQ, Lan HY. Challenges and recent advances in NK cell-targeted immunotherapies in solid tumors. *Int J Mol Sci* 2021; **23**:164.
19. Zhou ZK, Chen YF, Ba YH, Xu H, Zuo AN, Liu ST, et al. Revolutionising cancer immunotherapy: advancements and prospects in non-viral CAR-NK cell engineering. *Cell Prolif* 2025;**58**:e13791.
20. Zhang AQ, Yang XC, Zhang YC, Yu XX, Mu W, Wei J. Unlocking the potential of CAR-NK cell therapy: overcoming barriers and challenges in the treatment of myeloid malignancies. *Mol Cancer Ther* 2025;**24**: 536−49.
21. Sun HG, Zhu X, Lu PY, Rosato RR, Tan W, Zu YL. Oligonucleotide aptamers: new tools for targeted cancer therapy. *Mol Ther Nucleic Acids* 2014;**3**:e182.
22. Jbt McGivney, Csordas AT, Walker FM, Bagley ER, Gruber EM, Mage PL, et al. Strategy for generating sequence-defined aptamer reagent sets for detecting protein contaminants in biotherapeutics. *Anal Chem* 2018;**90**:3262−9.
23. Yang SH, Li H, Xu L, Deng ZH, Han W, Liu YT, et al. Oligonucleotide aptamer-mediated precision therapy of hematological malignancies. *Mol Ther Nucleic Acids* 2018;**13**:164−75.
24. Yang SH, Wen JG, Li H, Xu L, Liu YT, Zhao NX, et al. Aptamer-engineered natural killer cells for cell-specific adaptive immunotherapy. *Small* 2019;**15**:e1900903.
25. Zheng YS, Lai ZS, Wang B, Wei ZW, Zeng YY, Zhuang QY, et al. Natural killer cells modified with a Gpc3 aptamer enhance adoptive immunotherapy for hepatocellular carcinoma. *Discov Oncol* 2023;**14**: 164.
26. Santini FC, Rudin CM. Atezolizumab for the treatment of non-small cell lung cancer. *Expert Rev Clin Pharmacol* 2017;**10**:935−45.
27. Shah NJ, Kelly WJ, Liu SV, Choquette K, Spira A. Product review on the anti-PD-L1 antibody atezolizumab. *Hum Vaccin Immunother* 2018; **14**:269−76.
28. Liu R, Oldham RJ, Teal E, Beers SA, Cragg MS. Fc-engineering for modulated effector functions-improving antibodies for cancer treatment. *Antibodies* 2020;**9**:64.
29. Ullah I, Beaudoin-Bussières G, Symmes K, Cloutier M, Ducas E, Tauzin A, et al. The Fc-effector function of CIVID-19 convalescent plasma contributes to SARS-CoV-2 treatment efficacy in mice. *Cell Rep Med* 2023;**4**:100893.
30. Zhang A, Stacey HD, D'Agostino MR, Tugg Y, Marzok A, Miller MS. Beyond neutralization: Fc-dependent antibody effector functions in SARS-CoV-2 infection. *Nat Rev Immunol* 2023;**23**:381−96.
31. Cen J, Dai XY, Zhao H, Li XH, Hu XJ, Wu J, et al. Doxorubicin-loaded liposome with the function of "killing two birds with one stone" against glioma. *ACS Appl Mater Interfaces* 2023;**15**:46697−709.
32. Fu DJ, Ni Z, Wu KR, Cheng P, Ji XF, Li GY, et al. A novel redox-responsive ursolic acid polymeric prodrug delivery system for osteosarcoma therapy. *Drug Deliv* 2021;**28**:195−205.
33. Mu JQ, Zhong HP, Zou H, Liu T, Yu N, Zhang X, et al. Acid-sensitive PEGylated paclitaxel prodrug nanoparticles for cancer therapy: effect of peg length on antitumor efficacy. *J Control Release* 2020;**326**: 265−75.
34. Su ZY, Siak PY, Leong CO, Cheah SC. Nasopharyngeal carcinoma and its microenvironment: past, current, and future perspectives. *Front Oncol* 2022;**12**:840467.
35. Ding YX, Xiao XH, Zeng LL, Shang QP, Jiang W, Xiong S, et al. Platinum-crosslinking polymeric nanoparticle for synergetic chemo-radiotherapy of nasopharyngeal carcinoma. *Bioact Mater* 2021;**6**: 4707−16.
36. Lin QY, Zhou YQ, Ma J, Han SY, Huang YCX, Wu F, et al. Single-cell analysis reveals the multiple patterns of immune escape in the nasopharyngeal carcinoma microenvironment. *Clin Transl Med* 2023;**13**: e1315.
37. Gao SQ, Li TY, Guo Y, Sun CX, Xianyu B, Xu HP. Selenium-containing nanoparticles combine the NK cells mediated immunotherapy with radiotherapy and chemotherapy. *Adv Mater* 2020;**32**:e1907568.
38. Yang XH, Li CY, Yang HC, Li TW, Ling SS, Zhang YJ, et al. Programmed remodeling of the tumor milieu to enhance NK cell immunotherapy combined with chemotherapy for pancreatic cancer. *Nano Lett* 2024;**24**:3421−31.
39. Wang ZH, Shi ZZ, Liao XC, Quan GQ, Dong H, Zhao PN, et al. Broad-spectrum engineered multivalent nanobodies against SARS-CoV-1/2. *Adv Sci (Weinh)* 2024;**11**:e2402975.
40. Chen JJ, Qiu M, Ye ZF, Nyalile T, Li Y, Glass Z, et al. *In situ* cancer vaccination using lipidoid nanoparticles. *Sci Adv* 2021;**7**:eabf1244.
41. Wang JD, Ma JY, Xie FY, Miao FZ, Lv L, Huang YY, et al. Immunogenic cell death-based cancer vaccines: promising prospect in cancer therapy. *Front Immunol* 2024;**15**:1389173.
42. Kciuk M, Gielecińska A, Mujwar S, Kołat D, Kałuzińska-Kołat Ż, Celik I, et al. Doxorubicin-an agent with multiple mechanisms of anticancer activity. *Cells* 2023;**12**:659.
43. Petersen SH, Kua LF, Nakajima S, Yong WP, Kono K. Chemoradiation induces upregulation of immunogenic cell death-related molecules together with increased expression of PD-L1 and galectin-9 in gastric cancer. *Sci Rep* 2021;**11**:12264.
44. Sanchez CE, Dowlati EP, Geiger AE, Chaudhry K, Tovar MA, Bollard CM, et al. NK cell adoptive immunotherapy of cancer: evaluating recognition strategies and overcoming limitations. *Transplant Cell Ther* 2021;**27**:21−35.
45. Page A, Chuvin N, Valladeau-Guilemond J, Depil S. Development of NK cell-based cancer immunotherapies through receptor engineering. *Cell Mol Immunol* 2024;**21**:315−31.
46. Zhang D, Zheng YS, Lin ZG, Liu XL, Li J, Yang HH, et al. Equipping natural killer cells with specific targeting and checkpoint blocking aptamers for enhanced adoptive immunotherapy in solid tumors. *Angew Chem Int Ed Engl* 2020;**59**:12022−8.
47. Zhang D, Zheng YS, Lin ZG, Lan SY, Zhang XL, Zheng AX, et al. Artificial engineered natural killer cells combined with antiheat endurance as a powerful strategy for enhancing photothermal-immunotherapy efficiency of solid tumors. *Small* 2019;**15**:e1902636.
48. Chen ZP, Zeng WJ, Lei YM, Liang WB, Yang X, Yuan R, et al. Engineering of a multi-modular DNA nanodevice for spatioselective imaging and evaluation of NK cell-mediated cancer immunotherapy. *Angew Chem Int Ed Engl* 2025;**64**:e202414064.
49. Chen ZH, Zeng ZH, Wan QY, Liu XH, Qi JJ, Zu YL. Targeted immunotherapy of triple-negative breast cancer by aptamer-engineered NK cells. *Biomaterials* 2022;**280**:121259.
50. Tan JZ, Liu T, Fan WZ, Wei JL, Zhu BW, Liu YF, et al. Anti-PD-L1 antibody enhances curative effect of cryoablation *via* antibody-dependent cell-mediated cytotoxicity mediating PD-L1^{high}CD11b^{+}

cells elimination in hepatocellular carcinoma. *Acta Pharm Sin B* 2023; **13**:632−47.
51. Park JE, Kim SE, Keam B, Park HR, Kim S, Kim M, et al. Anti-tumor effects of NK cells and anti-PD-L1 antibody with antibody-dependent cellular cytotoxicity in PD-L1-positive cancer cell lines. *J Immunother Cancer* 2020;**8**:e000873.
52. Juliá EP, Amante A, Pampena MB, Mordoh J, Levy EM. Avelumab, an IgG1 anti-PD-L1 immune checkpoint inhibitor, triggers NK cell-mediated cytotoxicity and cytokine production against triple negative breast cancer cells. *Front Immunol* 2018;**9**:2140.
53. Birmpilis AI, Paschalis A, Mourkakis A, Christodoulou P, Kostopoulos IV, Antimissari E, et al. Immunogenic cell death, DAMPs and prothymosin α as a putative anticancer immune response biomarker. *Cells* 2022;**11**:1415.
54. Xie DQ, Wang QF, Wu GZ. Research progress in inducing immunogenic cell death of tumor cells. *Front Immunol* 2022;**13**: 1017400.
55. He Y, Zheng K, Qin XF, Wang SY, Li XJ, Liu HW, et al. Intravenous delivery of STING agonists using acid-sensitive polycationic polymer-modified lipid nanoparticles for enhanced tumor immunotherapy. *Acta Pharm Sin B* 2025;**15**:1211−29.
56. He K, Jia SG, Lou Y, Liu P, Xu LX. Cryo-thermal therapy induces macrophage polarization for durable anti-tumor immunity. *Cell Death Dis* 2019;**10**:216.
57. Zhao L, Yan F, Tang DH, Li WW, An N, Ren CX, et al. The transition between M1 and M2 macrophage phenotypes is associated with the disease status following CD19 CAR-T therapy for B cell lymphoma/leukemia. *Cell Death Dis* 2025;**16**:275.
58. Shen YJ, Yu N, Zhao WJ, Niu SN, Qiu P, Zeng HY, et al. M1-macrophage membrane-camouflaged nanoframeworks activate multiple immunity *via* calcium overload and photo-sonosensitization. *Biomaterials* 2025;**320**:123287.
59. Zhang RF, Shen YF, Zhou XY, Li JR, Zhao HQ, Zhang ZX, et al. Hypoxia-tropic delivery of nanozymes targeting transferrin receptor 1 for nasopharyngeal carcinoma radiotherapy sensitization. *Nat Commun* 2025;**16**:890.
60. Peng M, Zhang SS, Wu P, Hou XC, Wang D, Ge JS, et al. Circular RNA circCLASP2 promotes nasopharyngeal carcinoma progression through binding to DHX9 to enhance PCMT1 translation. *Mol Cancer* 2025;**24**:67.
61. Xie HJ, Zhang KW, Yin HM, Zhang SY, Pan S, Wu R, et al. Acetyltransferase NAT10 Inhibits T-cell immunity and promotes nasopharyngeal carcinoma progression through DDX5/HMGB1 axis. *J Immunother Cancer* 2025;**13**:e010301.
62. Mohan N, Hosain S, Zhao J, Shen Y, Luo X, Jiang JS, et al. Atezolizumab potentiates T cell-mediated cytotoxicity and coordinates with FAK to suppress cell invasion and motility in PD-L1$^+$ triple negative breast cancer cells. *OncoImmunology* 2019;**8**:e1624128.
63. Godiyal Y, Maheshwari D, Taniguchi H, Zinzuwadia SS, Morera-Díaz Y, Tewari D, et al. Role of PD-1/PD-L1 signaling axis in oncogenesis and its targeting by bioactive natural compounds for cancer immunotherapy. *Mil Med Res* 2024;**11**:82.
64. Luo LL, Wang S, Lang XL, Zhou TT, Geng J, Li XY, et al. Selection and characterization of the novel anti-human PD-1 FV78 antibody from a targeted epitope mammalian cell-displayed antibody library. *Cell Mol Immunol* 2018;**15**:146−57.